Effect of zinc incorporation on electron transport properties of indium oxide thin-film transistors

亜鉛導入が酸化インジウム薄膜トランジスタの電子輸送特性に及ぼす影響

Yuzhang Wu

Graduate School of Information Science and Technology

Hokkaido University

March 2025

Table of Contents

List of Figures

List of Tables

List of Acronyms

AFM	Atomic force microscopy
a-IZO	Amorphous Zn incorporated In_2O_3
ALD	Atomic layer deposition
AMOLED	Active-matrix organic light-emitting diode
CBM	Conduction band minimum
DOS	Density of states
EIL	Electron injection layer
EML	Emissive layer
ETL	Electron transport layer
GIXRD	Grazing incident X-Ray diffraction
HEMT(s)	High electron mobility transistor
HIL	Hole injection layer
HTL	Hole transport layer
ICP-MS	Inductively coupled plasma mass spectrometry

$IGZO_m$	$InGaZnO_{(3+m)}$
ITO	Indium tin oxide
IZO	Zn incorporated In_2O_3
LC	Liquid crystal
LCD	Liquid crystal display
NBS	Negative bias stress
OLED	Organic light-emitting diode
PBS	Positive bias stress
PLD	Pulse laser deposition
R.T.	Room temperature
RGB	Red, green, and blue
RMS	Root mean square
TFT(s)	Thin film transistor(s)
TOS	Transparent oxide semiconductor
TV	Television
XRD	X-Ray diffraction
XRR	X-Ray reflectance

List of Symbols

C_i	Capacitance of gate insulator
d	Thickness
E	Energy
e	Charge of electron
E_F	Fermi level
E_{inner}	Energy level of inner shell
E_{outer}	Energy level of outer shell
F_r	Fermi integral
g_m	Transconductance
h	Planck constant
I_{ab}	Current flow from a to b
I_{DS}, I_{ds}, $I_{d,}$,	Drain current
I_{off}	Off current of TFT
I_{on}	On current of TFT
$K1s$	$1s$ orbital of K shell
k_B	Boltzmann constant

$K\alpha 1$	*K*-alpha1 emission line
$K\alpha 2$	*K*-alpha2 emission line
$K\beta 1$	*K*-beta1 emission line
$K\beta 2$	*K*-beta2 emission line
L	Length of channel
$L2p_{3/1}$	1/2 spin states in *2p* orbital of *L* shell
$L2p_{3/2}$	3/2 spin states in *2p* orbital of *L* shell
m	Mass
m^*	Effective mass
m_0	Free Electron mass
$M3p_{1/2}$	1/2 spin states in *3p* orbital of *K* shell
$M3p_{3/2}$	3/2 spin states in *3p* orbital of *K* shell
m_d^*	Density of states effective mass
n	Carrier concentration
n_{2d}	Sheet carrier concentration
n_{3d}	Volume carrier concentration
q	Scattering vector
R	Resistance

r	Scattering parameter of the relaxation time
R_H	Hall coefficient
R_{sheet}	Sheet resistance
S	Thermopower / Seebeck coefficient
$S.S.$	Subthreshold swing
T	Temperature
t_{eff}	Effective channel thickness
V_{ab}	Voltage from a to b
V_{DS}, V_{ds}, V_d	Drain-source voltage
V_{GS}, V_g, V_{gs}	Gate-source voltage
V_{GSeff} V_{geff}	Effective gate voltage
V_{th}	Threshold voltage
W	Width of channel
$Zn\ a.t.\%$	Zn atomic ratio
$Zn\ w.t.\%$	Zn weight ratio
ΔT	Temperature difference
ΔV	Voltage difference / thermo-electromotive

	force
ε_r	Dielectric permittivity
λ	Wavelength
ξ	Chemical potential
f	Geometric factor
ΔV_{TH}	Threshold voltage shift
θ	Incident angel of X-Ray
μ_{FE}	Field-effect mobility
μ_{Hall}	Hall mobility
ρ	Resistivity
σ	Conductivity
τ	Relaxation time
ω	Incident angel of X-Ray

Chapter 1. General introduction

1.1 Background of this thesis

1.1.1 Display technique and Thin Film Transistor (TFT)

With the appearance of two foundational technologies, liquid crystal and light-emitting diodes, the modern display technologies, Liquid crystal display (LCD) and Organic light-emitting diode (OLED), were developed in the 1970s and 1980s. These innovations marked the beginning of a new era for visual communication. Since that more colorful and high-resolution displays became widely adopted in applications such as medical diagnostics, academic presentations, and entertainment, the ability to deliver information in a direct, effective manner significantly enhanced human life by improving efficiency and enjoyment [1,2].

Compared to OLEDs, LCDs offer several advantages. First, LCDs are generally more cost-effective to produce, especially for large-scale displays, due to mature manufacturing processes and widespread availability of raw materials[2]. Second, they provide excellent brightness levels, making them well-suited for environments with high ambient lighting[3]. Additionally, LCDs typically have a longer operational life as they are less susceptible to

issues like burn-in, which can occur in OLED panels after prolonged static image display [4,5]. Therefore, LCDs become a practical solution for many consumer and industrial applications

OLEDs, on the other hand, are becoming increasingly prevalent in premium consumer electronics and are poised to play a central role in the future of display technology.

Unlike LCDs relying on a backlight to illuminate pixels, OLED panels emit light directly from organic compounds when an electric current is applied. Therefore, OLEDs enable true black levels because individual pixels can be turned off completely, resulting in superior contrast ratios compared to LCDs. This feature is particularly beneficial for applications requiring high visual fidelity, such as professional video editing and high-end consumer displays. Second, OLED displays are thinner and more flexible, as they do not require a separate backlighting unit. This property has facilitated innovative designs in devices such as foldable smartphones and rollable televisions [6].

However, manufacturing costs of OLEDs remain relatively high, particularly for larger panels, due to the complexity of deposition processes and the need for advanced encapsulation technologies to protect organic materials from degradation Additionally, the issue of image retention, commonly referred to as burn-in, poses durability concerns in certain use cases [7-9].

1.1.2 Principle of display technique.

LCDs operate by modulating the passage of light through a liquid crystal (LC) layer, which changes its orientation in response to an applied electric field.

Figure 1 - 1 shows a schematic structure of LCD screen. The simplified structure contains a light source layer, an electrode layer often made of indium tin oxide (ITO), two mutually perpendicular polarizing filters, an alignment layer, and an LC layer. In each pixel, the liquid crystal molecules in liquid crystal layer are sandwiched between two mutually perpendicular polarizing filters and transparent electrodes. Without the LC layer, the polarizing light through the first polarizer would be blocked with the second polarizer layer. The alignment of LC was controlled with the on-off electric, which was modulated from the alignment layer composed of TFTs. Without an applied voltage, the liquid crystals are aligned in a way that switches the polarizing states of light, resulting in allowing light to pass through the second polarizers. When a voltage is applied, the molecular alignment is disturbed, blocking the light and darkening the pixel. The resulting grayscale or color image is achieved by adjusting the voltage across each pixel [2,10].

In addition, color in LCDs is achieved using red, green, and blue (RGB) color filters

placed over the sub-pixels within each pixel. By modulating the intensity of each sub-pixel, a full range of colors is produced via additive color mixing[2].

Figure 1 - 2 shows the schematic structure of OLED. OLED displays operate based on the principle of electroluminescence; wherein organic materials emit light in response to an electric current. The fundamental mechanism involves the injection, transport, and recombination of charge carriers within organic layers, resulting in the generation of excitons that decay radiatively to emit photons. The key layers in an OLED structure include the anode, cathode, and intermediate organic layers such as the hole injection layer (HIL), hole transport layer (HTL), emissive layer (EML), electron transport layer (ETL), and electron injection layer (EIL). Each layer is tailored to optimize charge carrier balance and recombination efficiency to produce high-quality light emission. In OLED display, TFT technology plays a critical role in enabling the operation of OLED displays by serving as the active-matrix backplane that drives and controls the pixels. In an active-matrix OLED (AMOLED) display, each pixel is independently controlled by an integrated TFT circuit, which typically consists of one or more transistors and capacitors. TFTs regulate the precise amount of current supplied to the organic emissive material, directly determining the brightness of each pixel. This current control is essential because the intensity of OLED emission is current-driven, and even slight variations in current

can result in significant differences in luminance.

1.1.3 Transparent oxide semiconductor

TFT with optical transparency is a critical device in controlling light through in LCD and OLED display in each pixel. Generally, TFT is composed of drain electrode, source electrode, gate electrode, gate insulator and semiconductor channel. Among them, one of the most critical parts for TFT performance is the semiconductor channel layer (**Figure 1 - 3 a**). In this regard, the increasing demand on resolution and respond speed of display required higher field-effect mobility of semiconductor channel layer. (**Figure 1 - 3 b**).

Currently, transparent oxide semiconductor (TOS)-based TFTs, represented by amorphous $InGaZnO_4$ ($IGZO_1$) TFTs, have been widely employed as the backplanes of active-matrix flat-panel displays of OLED and LCD TVs Since amorphous $InGaZnO_4$ TFTs exhibit one or two orders of magnitude higher field-effect mobility (μ_{FE} ~10 cm^2 V^{-1} s^{-1}) than that of previously used amorphous Si TFTs (μ_{FE} ~0.5 cm^2 V^{-1} s^{-1}), enabled higher pixel densities and reduced power consumption, essential for ultra-high-definition displays and wearable electronics. The reason why a-IGZO exhibited superior mobility is attributed to the ns-orbital conduction. In a-Si, the conduction band composed of sp3

orbital, which exhibit spatial directivity. Therefore, the strained chemical bonds in amorphous structures form rather deep and high-density localized states below conduction band minimum (CBM) and above valance band maximum (VBM) and thus behave as carrier trapping state. On the contrast, the CBMs of a-IGZO formed with the overlapping between spherically extended *s* orbitals of non-transition metal cations. The structural randomness and disorder in amorphous structure will not alter the overlapping much and thus exhibited less dependence with local structural randomness. This behavior led to a much smaller localized states in a-IGZO than a- Si[4,11] **(Figure 1 - 4).**

With a-IGZO channel, 4 K definition displays (3840 × 2160 pixels) with a frequency of 240 Hz single scan have been realized.[12]In the future, with an increasing demand for higher-definition display (8 K with 7680 × 4320 pixels) with high frequencies (480 Hz, single scan), TOS-TFTs that exhibit higher $\mu_{FE} \geqslant 50$ cm^2/V s would be required for pixel-driving circuits.

1.1.4 In_2O_3 based materials

Along with the discovery of IGZO, researchers focus on lots of transparent oxide semiconductors. Among numerous reports on TOS-TFTs showing higher μ_{FE} (> 50 cm^2

V^{-1} s^{-1}), In_2O_3 TFTs are considered a promising candidate because of their μ_{FE} (~100 cm^2 V^{-1} s^{-1}).[13] Crystalline In_2O_3 exhibits a cubic bixbyite structure (space group Ia3), characterized by a body-centered lattice with a lattice constant of approximately 10.1 Å. Since the drawbacks of pure In_2O_3-based TFT like commonly polycrystalline nature and oxygen vacancies, resulting in an impact on electric parameters such as mobility, stability and high threshold voltage. Therefore incorporate atoms to enhanced electric performance and stability is widely used such as Zn[14], Ga[15], Sn[16], Gd[17], etc. Among all of those atoms, the crystal became conducting when the value of overlap integral is larger than 0.4**(Figure 1 - 5).** The Zn become a good candidate due to Zn 4s orbital exhibited the closet over lapping integral with In5s and a wide bond angle from 80-140° while overlap integral larger than 0.4[15].

The lattice of Zn incorporated In_2O_3 (IZO, indium Zinc oxide) exhibited a hexagonal wurtzite crystal structure with space group R-3m. The lattice constant is proportional with Zn concentrations (**Figure 1 - 6**). With appropriate Zn contents, the material transit toward an amorphous state, which probably due to the more complex structure enhanced the energy requirement of nucleation. Amorphous IZO (a-IZO) lacks long-range periodicity but retains short-range order, a factor that contributes to uniformity and reduced grain boundary scattering in thin films.

Similar with IGZO, the conduction mechanism in In_2O_3-based materials primarily arises from the overlapping In5s-orbitals of indium atoms, which form a conduction band with low effective mass, resulting in relative high mobility in amorphous (**Figure 1 - 7**)[15]. Oxygen vacancies in In_2O_3-based materials serve as intrinsic donors, generating free carriers that contribute to n-type conductivity. The addition of Zn modifies the electronic structure by introducing Zn 4s orbitals, which participate in the conduction band. IZO exhibit a wide optical bandgap, typically ranging from 3.0 to 3.3 eV[18] depending on the indium-to-zinc ratio. This wide bandgap ensures high optical transparency in the visible spectrum, a critical property for optoelectronic applications such as TOS here.

Based on these properties, electrical properties of IZO can be tailored through compositional adjustments. The addition of Zn modulates carrier density and mobility. However, while Zn inclusion enhances material stability and reduces crystallization tendencies, excessive Zn content can disrupt the conduction pathways, reducing carrier mobility. Though Zn 4s orbital also contributes to conduction band, there are still a lot of factors disturbing and thus the balance of them is necessary to be discovered.

1.2 Objective of this thesis

The aim of this doctoral research is systematically investigating the effect of Zn

incorporation into In_2O_3 films and thin film transistor on crystallinity, electron transport properties, and effective thickness.

This thesis is organized in the following way.

In chapter 1, the background and objective of this research are introduced.

In chapter 2, analysis method and technology of structure, electron transport properties, and TFT performance are mainly introduced.

In chapter 3, the structural and electrical properties of IZO films with varying Zn concentration and annealing conditions are explored.

In chapter 4, I detailed investigate the electrical transport properties of 300 ºC annealed IZO films and TFTs across a wide range of Zn concentrations, which correspond different crystallized nature.

In chapter 5, electric field thermopower modulation analyses were proceeded to observed changes in effective channel thickness (t_{eff}) of amorphous and polycrystalline IZO TFTs as a function of effective gate voltage (V_{GSeff}), and so that investigate the operating mechanism in different crystallinity.

In chapter 6, the present study is summarized.

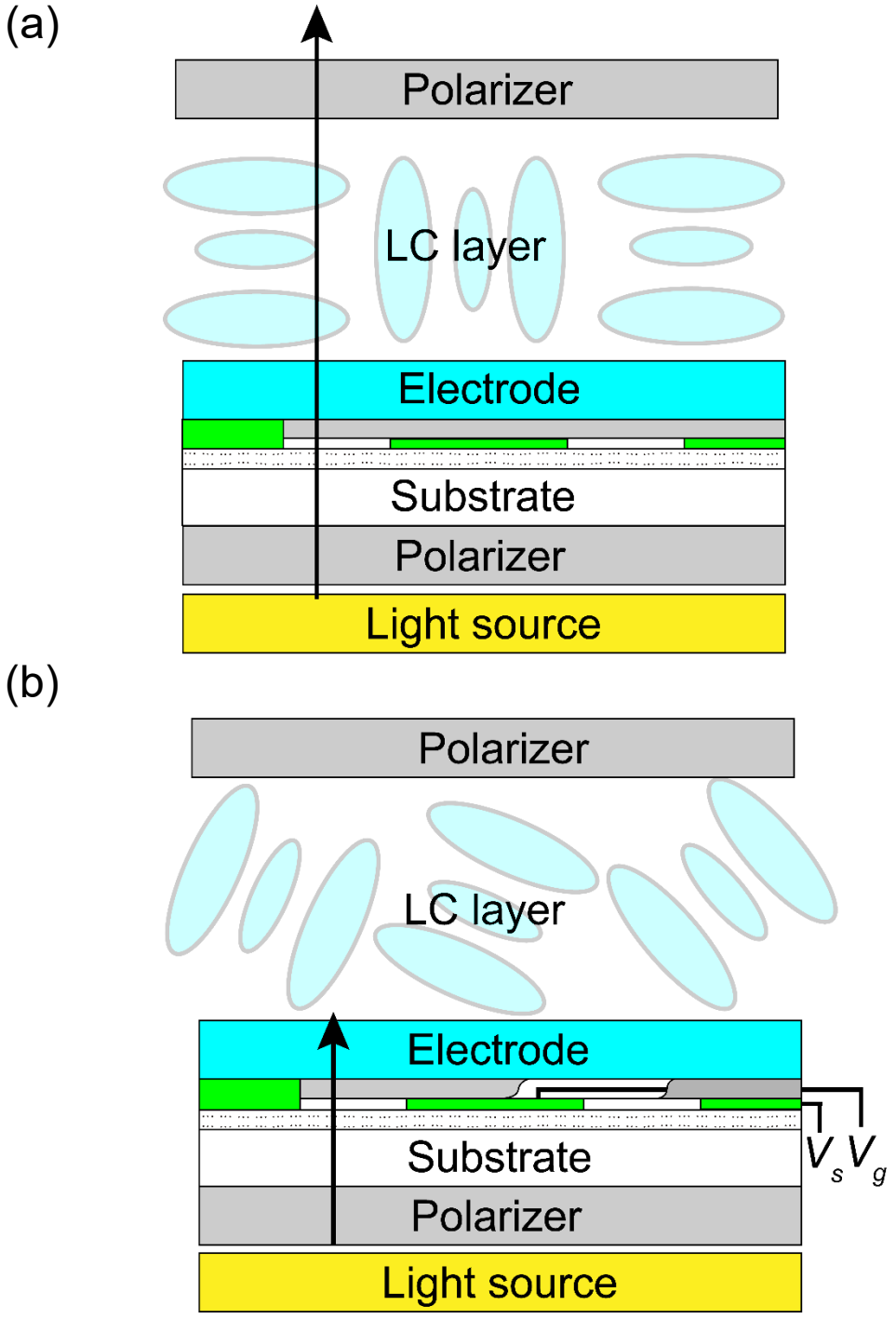

Figure 1 - 1 Schematic of one pixel in LCD display and the operating principle.

(a): The pixel worked without electricity

(b): The pixel darked with electricity

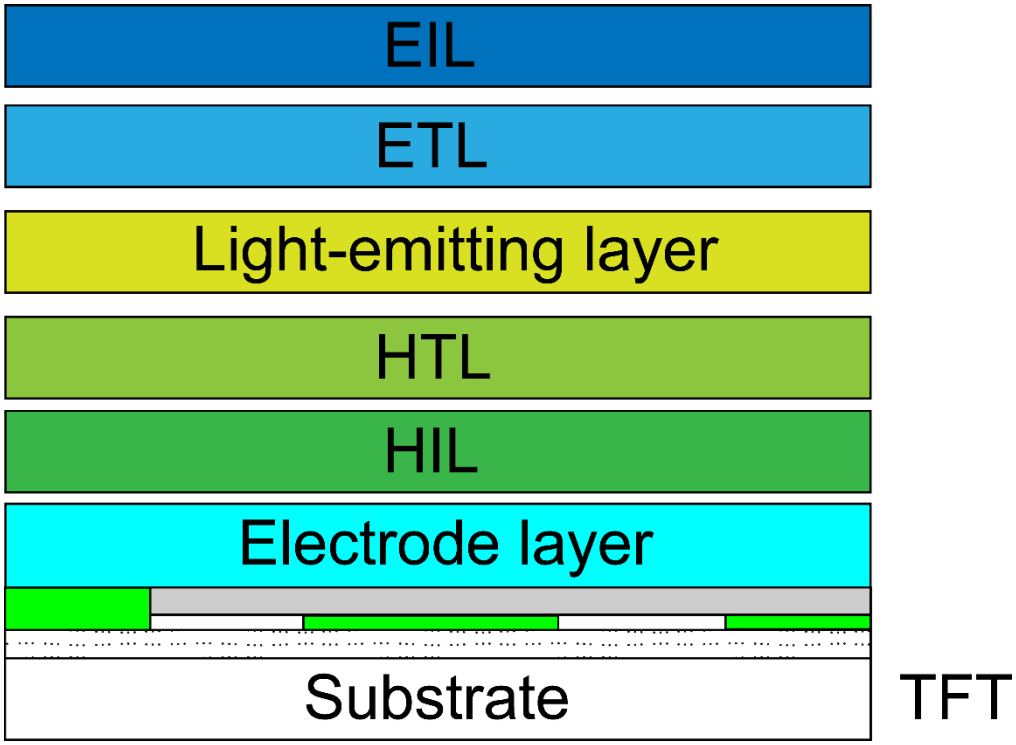

Figure 1 - 2 Schematic structure of one pixel in OLED display

Each pixel is independently controlled by an integrated TFT circuit

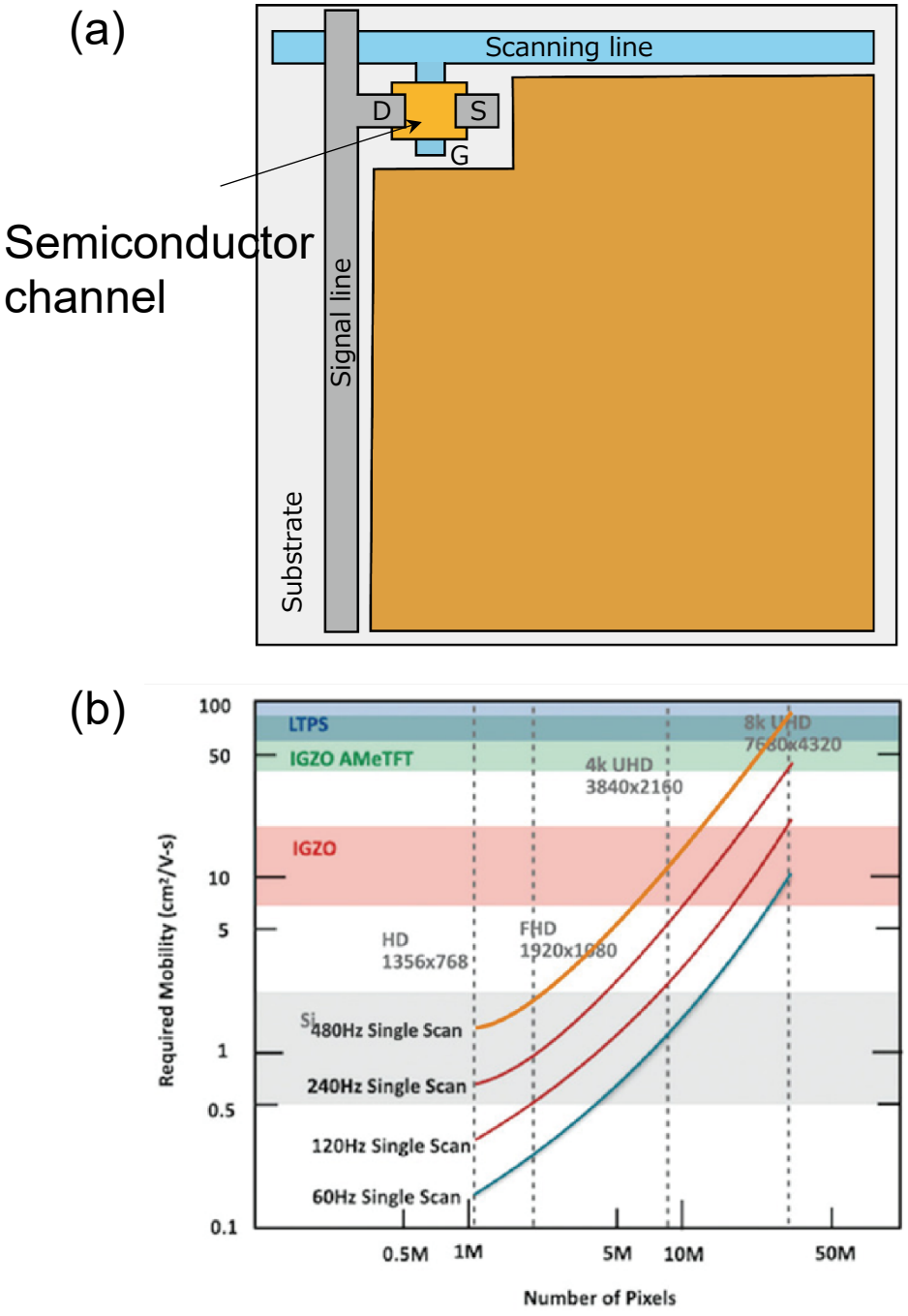

Figure 1 - 3 (a)schematic of TFT in display technology (b)The required field-effect mobility for various delivers pixel number, resolution and scanning speed in display technique[19]

.

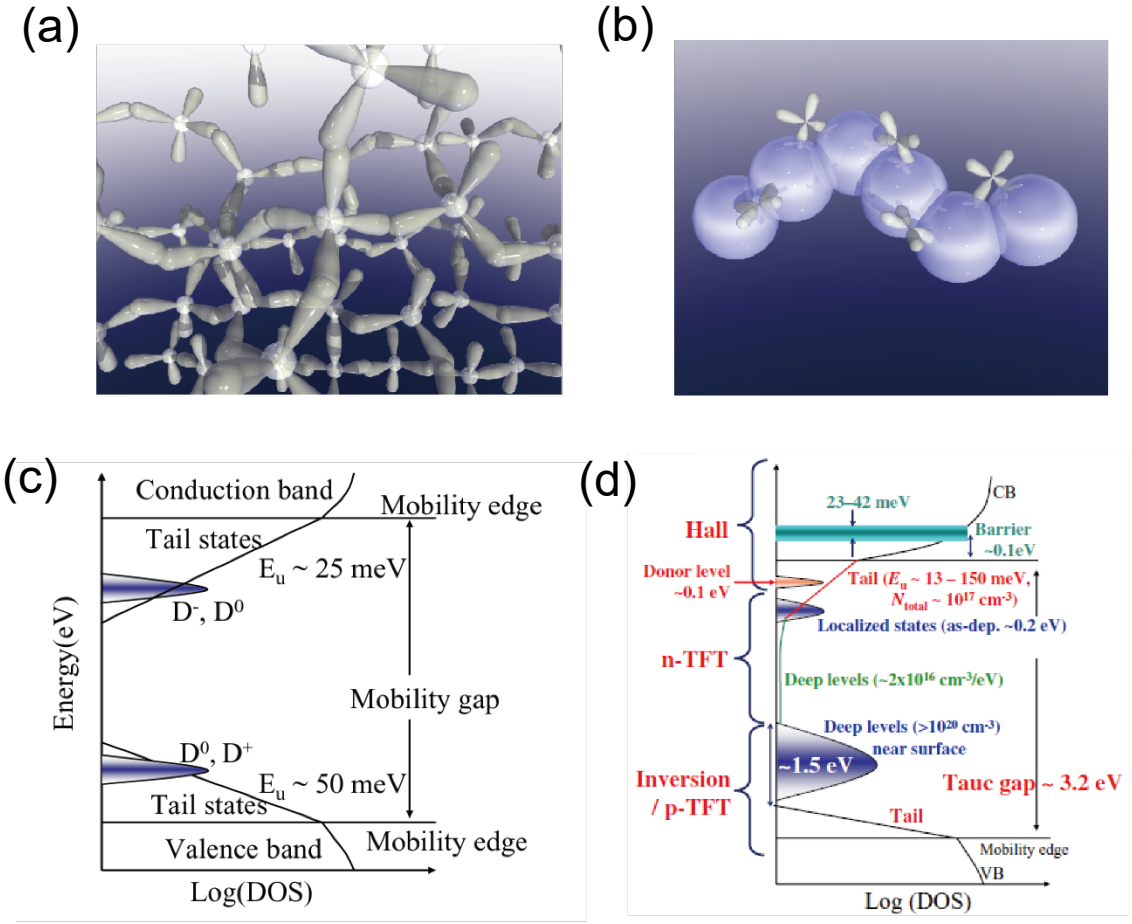

Figure 1 - 4 Schematic orbital of carrier's pathway and band structure of a-Si and a-IGZO

(a, c) a-Si

(b, d) a-IGZO[4,11]

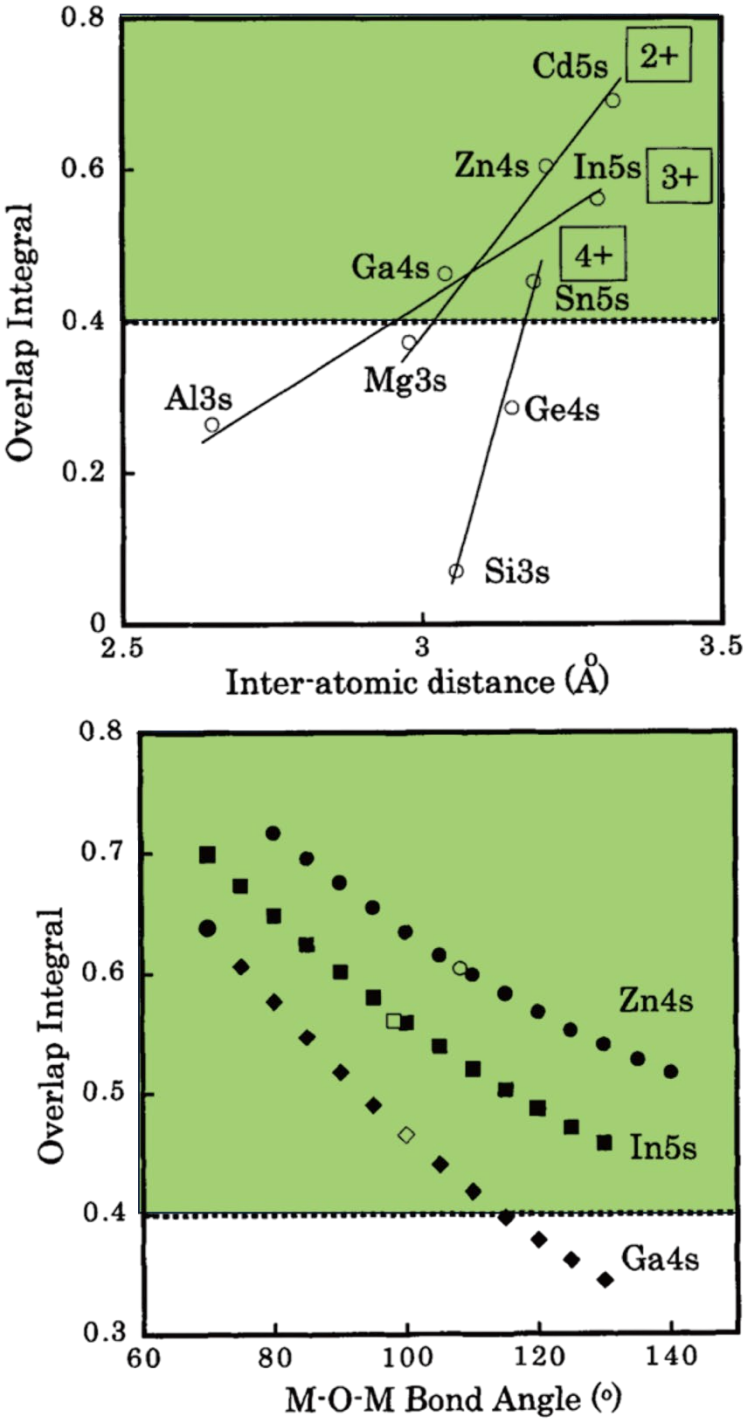

Figure 1 - 5 Calculated overlap integral of s-orbital as function of the inter-atomic distance between 2 nearest metal ions and M-O-M bond angle.[15]

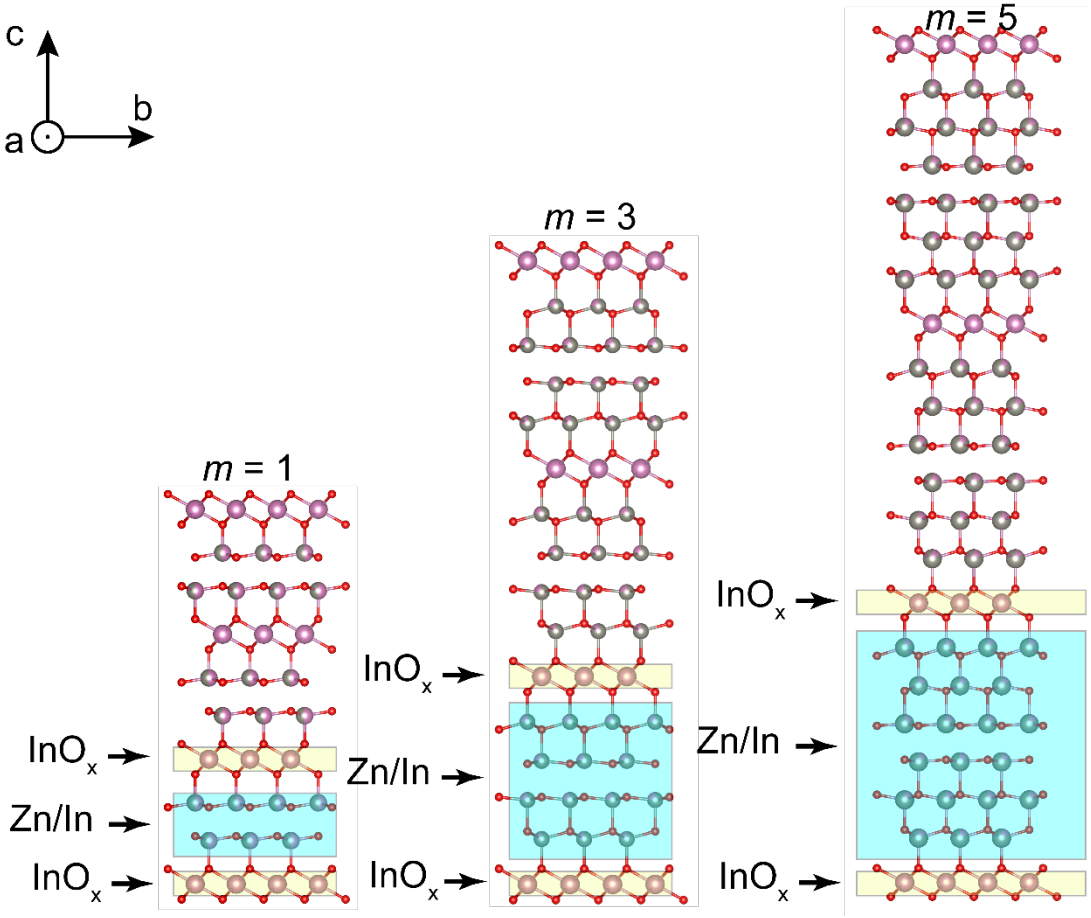

Figure 1 - 6 Schematic structure of crystalized $In_2O_3(ZnO)_m$ (m = 1, 3, 5)

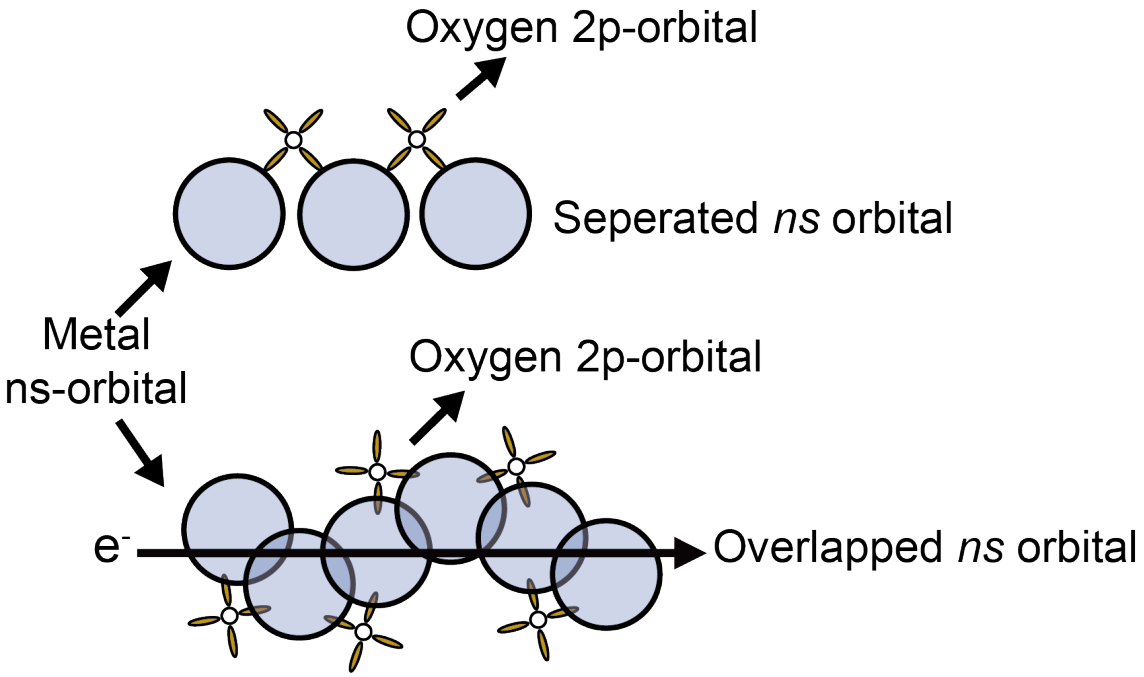

Figure 1 - 7 Schematic *s* orbital overlapping between *(n - l)* $d^{10}ns^0$ metal atoms. [15]

Reference

[1] Castellano, J. A. *Liquid gold: the story of liquid crystal displays and the creation of an industry*. World Scientific, (2005).

[2] Kawamoto, H. The history of liquid-crystal displays. *Proceedings of the IEEE* **90**, 460-500 (2002).

[3] Yang, Z., Hsiang, E.-L. *et al.* Performance comparison between mini-LED backlit LCD and OLED display for 15.6-inch notebook computers. *Applied Sciences* **12**, 1239 (2022).

[4] Nomura, K., Ohta, H. *et al.* Room-temperature fabrication of transparent flexible thin-film transistors using amorphous oxide semiconductors. *nature* **432**, 488-492 (2004).

[5] Guo, Z., Liu, C. *et al.* in *2023 International Conference on Electrical Engineering and Photonics (EExPolytech).* 163-166 (IEEE).

[6] Forrest, S. R. The path to ubiquitous and low-cost organic electronic appliances on plastic. *nature* **428**, 911-918 (2004).

[7] Tang, C. W. & VanSlyke, S. A. Organic electroluminescent diodes. *Applied physics letters* **51**, 913-915 (1987).

[8] Hsiang, E. L., Yang, Z. *et al.* Prospects and challenges of mini-LED, OLED, and micro-LED displays. *Journal of the Society for Information Display* **29**, 446-465 (2021).

[9] Huang, Y., Hsiang, E.-L. *et al.* Mini-LED, Micro-LED and OLED displays: present status

and future perspectives. *Light: Science & Applications* **9**, 105 (2020).

[10] Bahadur, B. Liquid crystal displays. *Molecular crystals and liquid crystals* **109**, 3-93 (1984).

[11] Kamiya, T., Nomura, K. *et al.* Present status of amorphous In-Ga-Zn-O thin-film transistors. *Sci Technol Adv Mater* **11**, 044305 (2010).

[12] Hendy, I., Brewer, J. *et al.* Development of Xhigh-performance IGZO backplanes for dxisplays. *Information Display* **38**, 60-68 (2022).

[13] Magari, Y., Kataoka, T. *et al.* High-mobility hydrogenated polycrystalline In2O3 (In2O3: H) thin-film transistors. *Nature communications* **13**, 1078 (2022).

[14] Paine, D. C., Yaglioglu, B. *et al.* Amorphous IZO-based transparent thin film transistors. *Thin solid films* **516**, 5894-5898 (2008).

[15] Orita, M., Ohta, H. *et al.* Amorphous transparent conductive oxide InGaO3 (ZnO) m (m≤ 4): a Zn4s conductor. *Philosophical magazine B* **81**, 501-515 (2001).

[16] Yang, H., Zhang, Y. *et al.* Thermopower Modulation Analyses of High-Mobility Transparent Amorphous Oxide Semiconductor Thin-Film Transistors. *Acs Appl Electron Ma* **4**, 5081-5086 (2022).

[17] Lee, S.-H., Kim, T. *et al.* Solution-processed gadolinium doped indium-oxide thin-film transistors with oxide passivation. *Applied Physics Letters* **110** (2017).

[18] Ishida, T., Nishimura, T. *et al.* Tunable-Conduction-Band In–Zn–O-Based Transparent Conductive Oxide Deposited at Room Temperature. *physica status solidi (a)* **219**, 2200061 (2022).

[19] Hendy, I., Brewer, J. *et al.* Development of high-performance IGZO backplanes for displays. *Information Display* **38**, 60-68 (2022).

Chapter 2. Experiment method

2.1 Pulse laser deposition

Pulsed laser deposition (PLD) was a typical method of physical vapor deposition (PVD) method, which exhibits great controllability and relatively high with deposition rate. A schematic representation of the process, utilizing a KrF excimer laser (λ=248 nm) is shown in **Figure 2 - 1**.

The film growth mechanism in PLD could be divided into several step, in which contains complex physical and chemical process:

1. A high-power laser pulse ablates the target material.
2. The target was rapidly vaporized and generated a plasma plume within a vacuum chamber.
3. Particles in the plasma are transported and condensed onto a substrate, forming nucleation and occur the film growth.

The quality of thin films produced through PLD is influenced by several key factors. The laser parameters, which include wavelength, pulse energy and repetition rate, significantly affect the ablation process and the formation of the plasma plume. Substrate temperature also plays critical roles in governing the kinetic energy and mobility of the

ablated species, which directly impacts the nucleation and growth dynamics. Furthermore, the target composition and surface conditions influence the stoichiometry and uniformity of the resultant film. The parameters of atmosphere such as gas composition and pressure also play an important role in the composition of resultant film. Optimizing these parameters forming a proper conditions is essential to achieve high-quality films with desired physical and chemical properties. [1]

In this research, all IZO films species, ITO electrode of source and drain in TFT, Y_2O_3 passivation layer was deposited with PLD in oxygen at room temperature (R.T.).

2.2 Surface morphology with AFM

Atomic force microscopy (AFM) is a powerful and versatile technique widely used in materials science, nanotechnology, and biological research to investigate surface topography at the nanoscale. It operates with measuring the interaction forces between a sharp probe tip and the sample surface, providing high-resolution imaging and quantitative data.

The schematic AFM structure was shown in **Figure 2 - 2**. A sharp tip mounted on a cantilever to scan a sample surface. The tips interact with the surface, altering numerous

forces (e.g., van der Waals, electrostatic, or magnetic) then cause the cantilever to deflect. These deflections are detected using a laser beam reflected off the cantilever onto a photodetector and transfer into optical information, which is then processed to create high-resolution 3D images of the surface.[2]

In this research, AFM (Nanocute, Hitachi High-Tech Sci. Co) was utilized as a surface morphology photographer to estimate surface roughness.

2.3 Crystallinity with XRD

X-Ray diffraction (XRD) is a non-destructive analytical technique used to determine the atomic and molecular structure of crystalline materials. By measuring the optical properties such as intensity of X-rays scattered off the periodic arrangement of atoms in a sample, XRD provides information about structural properties including crystallographic structure, phase composition, lattice constant, etc.

Figure 2 - 3 a simply exhibited the principle of X-ray generation. First, the electrons are drawn out from a heating filament (always tungsten). The electron gains sufficient kinetic energy between 2 electrodes with high electric potential difference of several decades kV, then losing kinetic by collision with anode (metal target, *Cu*, in this research).

The losing kinetic energy of electrons converts into heat and excites the inner-shell electrons in the anode and generates pairs of an outer electron and a hole. The excited electrons release energy as X-Ray photons with energy $E = E_{outer} - E_{inner}$, where E_{outer} and E_{inner} represent outer shell energy level and inner shell energy level. The X-Ray was divided into $K\alpha 1$, $K\alpha 2$, $K\beta 1$, $K\beta 2$ etc., corresponding to the X-ray emission from the recombination that $L2p_{3/2} - K1s$, $L2p_{1/2}$ - $K1s$, $M3p_{3/2}$ - $K1s$ and $M3p_{1/2}$ - $K1s$ respectively.

Figure 2 - 3 c shows the schematic alignment of XRD properties. The generated X-ray was filtered with collimation consists of monochromator formed with Ge (220) crystal and soller slits. The collimated X-ray with single wavelength incident the samples on flat plate and causes Bragg's diffraction**(Figure 2 - 3 b)**, which follows Bragg's Law[3]:

$$n\lambda = 2dsin\theta$$

where n, λ, d, θ represented wave number, wavelength, thickness and incident angel here. The equation was derived from the X-ray path difference between photons reflected at the upper and lower lattice plane, which is consistent with diffracting condition. The diffracted X-ray was collimated again and detected with an X-ray detector. Characteristic peak was able to be observed for every θ and d consistent with Bragg's law.

In addition, there is XRD equipment utilized a fixed X-ray generator for engineering reason, resulting in the incident angle geometrically equal to the rotating angle of the

sample plate and marked as θ *or* ω. Consistent with the geometric relationship, the angle between X-ray detector and flat plane (note as dot line in **Figure 2 - 3 c.** was 2 times of θ. This is the reason why the out-of-plane XRD method was also named as "$\omega - 2\theta$ scan" or "$\theta - 2\theta$ scan".

Normally, a sample with high crystallinity is easy to observe clear peaks, due to the long-range orderly lattice arrangement strongly diffract X-ray (**Figure 2 - 3 d).** For amorphous with so-called short-range orderly arrangement or polycrystalline with tiny grain size, the grazing incident X-Ray diffraction (GIXRD) method was utilized. With this method, the X-ray incident in a fixed small angle (≤ 1.0°). The intensity of resultant peaks will enhance a lot and so that able to observe amorphous phase (**Figure 2 - 3 e**). For instance, **Figure 2 - 3 f** exhibited a GIXRD pattern of amorphous(m = 1-4) and crystallized (m = 5) $IGZO_m$ film[4]. The halo peaks at ~22° and 34° arise from amorphous phase Si substrate and $IGZO_m$ film (m < 5, integer) respectively, and the sharp peaks at 32° represent crystalline phase of $IGZO_m$ (m = 5) film.

The thickness of films was able to observe with X-Ray reflectance (XRR) method. With a small, fixed θ, the X-Ray reflected at surface and bottom and interfered with each other, which was observed as interference fringes when proceeding $\omega - 2\theta$ scan (**Figure 2 - 4**). For analyzing XRR pattern, the film thickness d is calculated from the

periodicity of interference fringes, as it is inversely proportional to their spacing. The overall slope of the reflectivity curve provides information about surface and interface roughness, while the critical angle reveals the density of the material. The fringes amplitude reveals the density contrast. For instance, in the 2-layer structure case, the density contrast was determined by film and substrate.

In this research, the utilized X-Ray is $K\alpha 1$ beam generated with K shell of Cu target. The $\omega - 2\theta$ scan and GIXRD was utilized to determine crystallinity and composition. Film thickness was measuring with XRR.

2.4 Hall measurement

Hall measurement using four probes is a widely adopted technique for evaluating the electrical properties of thin films. Depending on the probe alignment, the two most employed methods are the Van der Pauw method and the four-point probe method.

In the Van der Pauw method **(Figure 2 - 5 left)**, probes are positioned at the four corners of the film (e.g., Probe 1–4). The current flowing along one edge and the voltage across the opposite edge are denoted as with I_{ab} (current flow from corner a to b, e.g. I_{12}) and V_{ab} (Voltage from a to b, e.g. V_{34}) respectively. Measurements can similarly be made

along the diagonals. This configuration enables the determination of the corresponding resistances with following equation:

$$R_{12,34} = \frac{V_{34}}{I_{12}}$$

$$R_{23,14} = \frac{V_{23}}{I_{14}}$$

Based on $R_{12,34}$ and $R_{23,14}$ the resistivity can be readily calculated by incorporating geometry parameters.

$$\rho = \frac{\pi d}{ln2}\left(\frac{R_{12,34} + R_{23,41}}{2}\right) f$$

$$\frac{R_{12,34} - R_{23,41}}{R_{12,34} + R_{23,41}} = \frac{f}{ln2} arccosh(\frac{1}{2}\exp(\frac{ln2}{f}))$$

where d is the thickness of films, f is a geometric factor. For a symmetric specimen, the f factor equal to 1.

Additionally, the sheet resistance is determined as

$$R_{sheet} = \frac{R}{d}$$

The electric transport properties in semiconductor such as carrier concentrations n, Hall mobility was also able to measure from Hall measurement, which are represented with following equations

$$\sigma = \frac{1}{\rho} = n\mu_e e + p\mu_{hole} e$$

where n, p, μ_e , μ_{hole} represents electron concentration, hole concentration, electron mobility and hole mobility respectively.

Hall mobility could be calculated with following equations

$$\mu = e\sigma R_H$$

The Van der Pauw method particularly requires isotope of materials due to the difference mearing line of voltage and current. If the specimen exhibited anisotropic electron transport properties, a four-point probe method is the solution. **(Figure 2 - 5 right)** Current and Voltage were measured with probes 1,4 and probes 2,3 respectively, which are aligned in a line.

In this research, electron transport properties were measured with d.c. four probe equipment with Van der Pauw arrangement at R.T. in air. In order to advance contacting performance, In-Ga alloy was utilized as contacting electrodes.

2.5 Electric transfer and output characteristic of TFT

TFT operate based on the field-effect principal (**Figure 2 - 6 a**), where an electric field applied through the gate electrode modulates the conductivity of a semiconductor channel, allowing precise control over current flow between the source and drain electrodes.

TFT electrical properties are characterized using transfer and output curves, which provide essential insights into their performance.

The transfer curve(**Figure 2 - 6 b**), obtained by plotting the drain current I_{DS} versus the gate-source voltage V_{GS} at a fixed drain-source voltage V_{DS}, reveals key parameters such as the threshold voltage V_{th}, subthreshold swing *S.S.* , and the on-off current ratio $\frac{I_{on}}{I_{off}}$. As definition, V_{th} can be extracted as the V_{GS} at which a significant increase in current begins. The *S.S* was extracted from V_{GS}, which required an increase in the drain current (I_{DS}) from 1 to 10 pA. The field-effect mobility provides an important description on the ability of carriers' transportation in channel. In the saturation region, the drain current can be evaluated by:

$$I_{DS} = \frac{1}{2}\,\mu_{FE} C_i \frac{W}{L}\,(V_{GS} - V_{TH})^2$$

where *W* and *L* correspond to the width and length of channel. To simplify the calculation and suppress the operating difficulties, transconductance g_m determined from the $\frac{\partial I_{DS}}{\partial V_{GS}}$ was utilized in field-effect mobility calculation as following equation.

$$\mu_{FE} = g_m \frac{2L}{WC_i}$$

Another calculation method is measuring the on-current at saturation region as following:

$$\mu_{FE} = \frac{\left(d\sqrt{I_d}/dV_g\right)^2}{(W/2L)C_i},$$

The output curve (**Figure 2 - 6 c**), which plots I_{DS} versus V_{DS} at different V_{GS}, is

used to analyze the TFT's operation in the linear and saturation regions. In the linear region, the drain current depends linearly on V_{DS}, while in the saturation region, I_{DS} becomes independent of V_{DS} , indicating a pinch-off at the drain end of the channel. From these curves, physical quantities such as the on-current, off-current, saturation drain current, and contact resistance can also be extracted, enabling comprehensive evaluation of the device's performance for various applications. In applications, TFT always works under saturation region.

The stability of TFT was characterized by Negative Bias Stress (NBS) and Positive Bias Stress (PBS) testing. NBS and PBS are reliability evaluation methods used to study the stability of thin-film transistors (TFTs) under prolonged electrical stress. In detail, a constant negative/positive gate bias is applied to the device for an extended period under typically controlled environmental conditions. The resulting variation in electrical characteristics, such as threshold voltage shift ΔV_{TH}, highly depends on charge trapping mechanisms, interface quality, and material degradation within the gate dielectric or semiconductor layer. Particularly, NBS is relevant for understanding device performance under operational stress conditions.

In this research, TFT performance parameters such as V_{TH}, *S.S.* etc. were evaluated with transfer curve and output curve. V_{TH} was directly observed when I_{ds} = 10nA, the

field-effect mobility was calculated in saturation region with transconductance. The PBS and NBS were measured under same applied electric field with ±2 MV/cm.

2.6 Thermopower measurements and thermopower modulation

Thermopower, or the Seebeck coefficient, is a critical parameter that measures the voltage induced by a temperature gradient across a material. It is formally defined as:

$$S = -\frac{\Delta V}{\Delta T}$$

where ΔV is the voltage difference and ΔT is the temperature difference. A positive thermopower indicates that the majority carriers are holes, while a negative thermopower suggests electrons as the dominant charge carriers. Thermopower is highly sensitive to the density of states (DOS) near the Fermi level E_F and is influenced by scattering mechanisms and carrier type. Therefore, it could be understood that thermopower is a factor associated with electric transport properties and structure. Experimentally, the thermopower was measured through the voltage difference at the cool side and hot side of sample (**Figure 2 - 7 a**).

From the perspective of carrier transport, the relationship between thermopower and carrier concentration can be quantitatively described by the Mott equation, which relates

thermopower to the energy dependence of conductivity at the Fermi level:

$$S = -\frac{\pi^2}{3}\frac{k_B^2 T}{e}\left\{\frac{d\left[\ln\left(\sigma(E)\right)\right]}{dE}\right\}_{E=E_F}$$

where k_B is the Boltzmann constant, T is the absolute temperature, e is the elementary charge, and σ is the energy-dependent electrical conductivity.

When E close to E_F, conductivity could be expressed as

$$\sigma(E) \propto DOS(E)v^2(E)\tau(E)$$

where DOS is density of states, v is the electron speed, τ is relaxation time. Substitute into the above formula, Seebeck coefficient could be simplified expressed as

$$S \propto -\frac{k_B}{e}\cdot\frac{1}{DOS(E_F)}\left[\frac{\partial DOS(E)v^2(E)\tau(E)}{\partial E}\right]_{E=E_F}$$

If E_F closed to conduction band minimum, the density of states is nearly constant near the Fermi level, thus $v = \frac{\partial E}{\partial k}$ is closed to fermi velocity. τ was also evaluated to constant due to it is mainly determined by the Pauli exclusion principle and density of states near CBM. Therefore, the slope in $\frac{\partial DOS(E)}{E}$ vs E plot represent the Seebeck coefficient. Due to the position of fermi level, the thermopower exhibited negative value in n-type semiconductor and positive value in p-type semiconductor. (**Figure 2 - 7 b**).

There is another analysis method named jonker plot is S – log n plot. The effective mass m^* could be calculated from following equations:

$$n_{3D} = 4\pi\left(\frac{2 \cdot m_d^* \cdot k_B \cdot T}{h^2}\right)^{\frac{3}{2}} F_r(\xi)$$

$$F_{\mathrm{r}}(\xi) = \int_0^{\infty} \frac{x^r}{1 + e^{x-\xi}} dx$$

$$S = -\frac{k_{\mathrm{B}}}{e}\left(\frac{(r+2)F_{\mathrm{r}+1}(\xi)}{(r+1)F_{\mathrm{r}}(\xi)} - \xi\right)$$

where n_{3d}, m_{d}*, k_{B}, T, h, ξ, F_{r}, and r are the volume carrier concentration, the density of states effective mass (m_{d}* = spin degeneracy × m* = 2m*), Boltzmann constant, absolute temperature, Planck constant, chemical potential, Fermi integral, and scattering parameter of the relaxation time, respectively. Without constants, the various contains n_{3D}, m_{d}*, ξ, F_{r}. Among them, ξ, F_{r} are a set of coupled parameters independent with others, and the carrier concentrations of films would be measured from Hall measurement. Therefore, the m* of films can be easily simulated.

Thermopower modulation is a technique used to determine the t_{eff} of a TFT. As an extension of the thermopower measurement, thermopower modulation provides an effective means of determining t_{eff} based on the relationship

$$t_{eff} = \frac{n_{2D}}{n_{3D}}$$

In this method, the S is measured simultaneously with the modulation of the gate voltage V_{GS} of the TFT (**Figure 2 - 8 a**), which controls carrier transport in the channel through the field effect. The three-dimensional carrier concentration n_{3D} is derived from

the measured Seebeck coefficient, while the two-dimensional carrier concentration n_{2D} is obtained from the sheet carrier density n_s using the relation

$$n_s = C_i(V_{GS} - V_{TH})$$

where C_i is the gate capacitance per unit area and V_{TH} is the threshold voltage. This combined approach enables precise determination of the effective thickness and provides insights into the carrier transport behavior of the TFT.

As reference, the effective channel thickness of commonly discussed material such as $BaSnO_3$-TFTs, SnO_2-TFTs, and AlGaN/GaN HEMTs. was characteristic with this method named "Electric field thermopower modulation analysis" method. [5-10]

In this research, S was measured at R.T. by creating a ΔT of ~10 K using two Peltier devices. The thermo-electromotive force (ΔV) and ΔT were measured simultaneously, and the S-values were obtained from the slope of the $\Delta V - \Delta T$ plots. Thermopower modulation was proceeded with 2 two Peltier devices to generate temperature gradient. The temperature difference was monitored with two K-type thermocouples (150 μm in diameter, SHINNETSU Co.). As schematically shown in **Figure 2 - 8 b**, for an n-type channel, if V_{GS} (1) < V_{GS} (2), generally, observable $|S|$ at low V_{GS} (1) is larger than that at high V_{GS} (2).

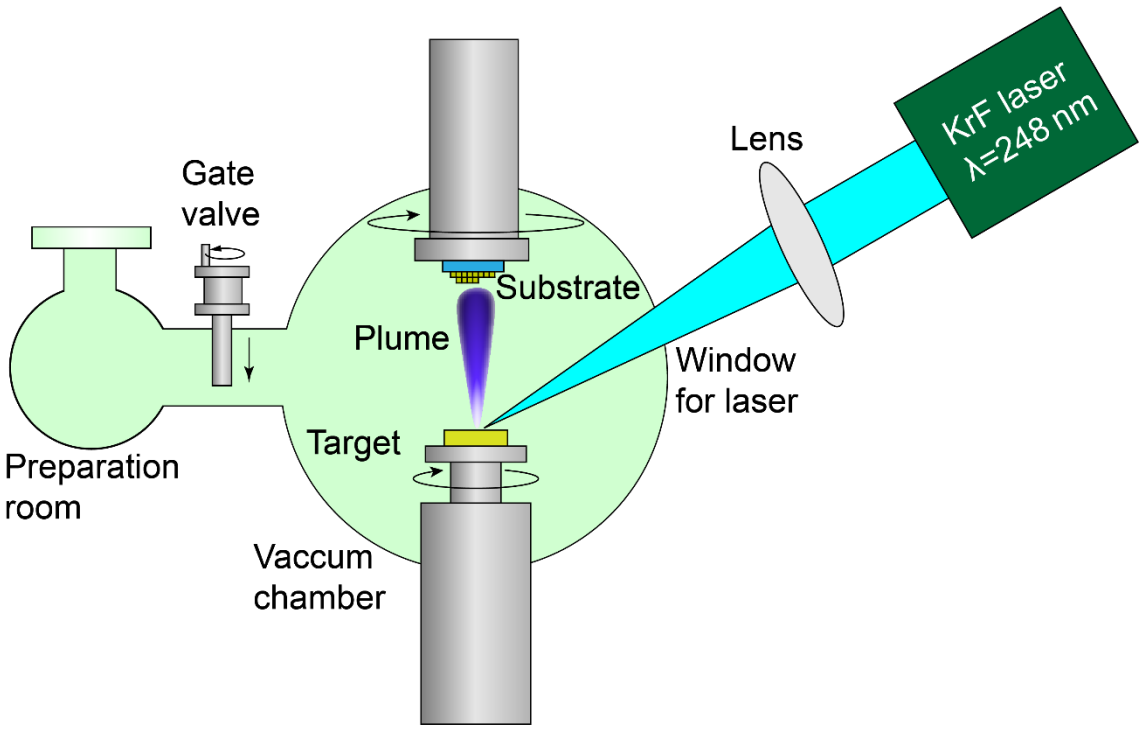

Figure 2 - 1 Schematic figure of pulse laser deposition (PLD) system and ablation of target

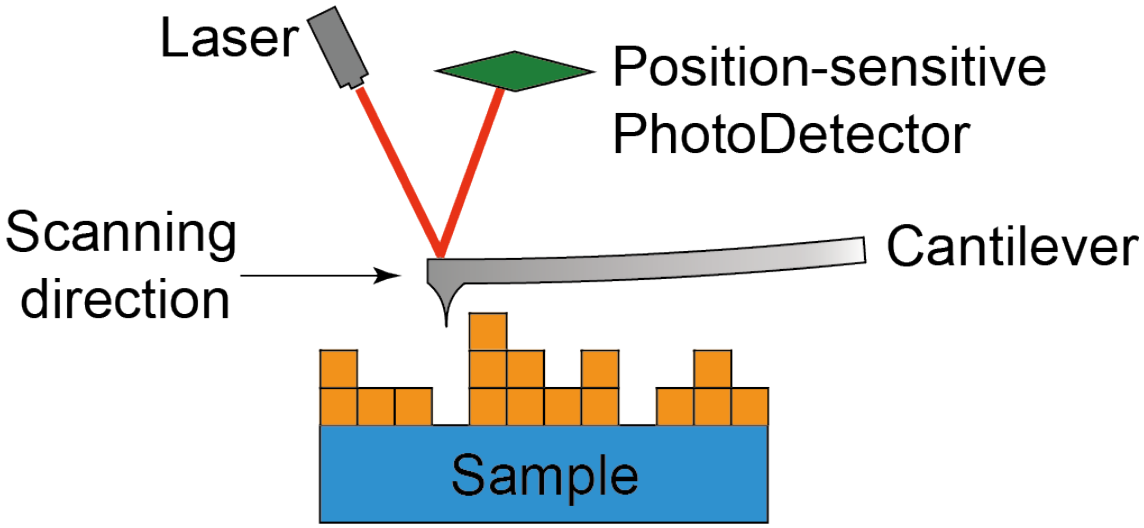

Figure 2 - 2 Schematic structure of atomic force microscopy (AFM)

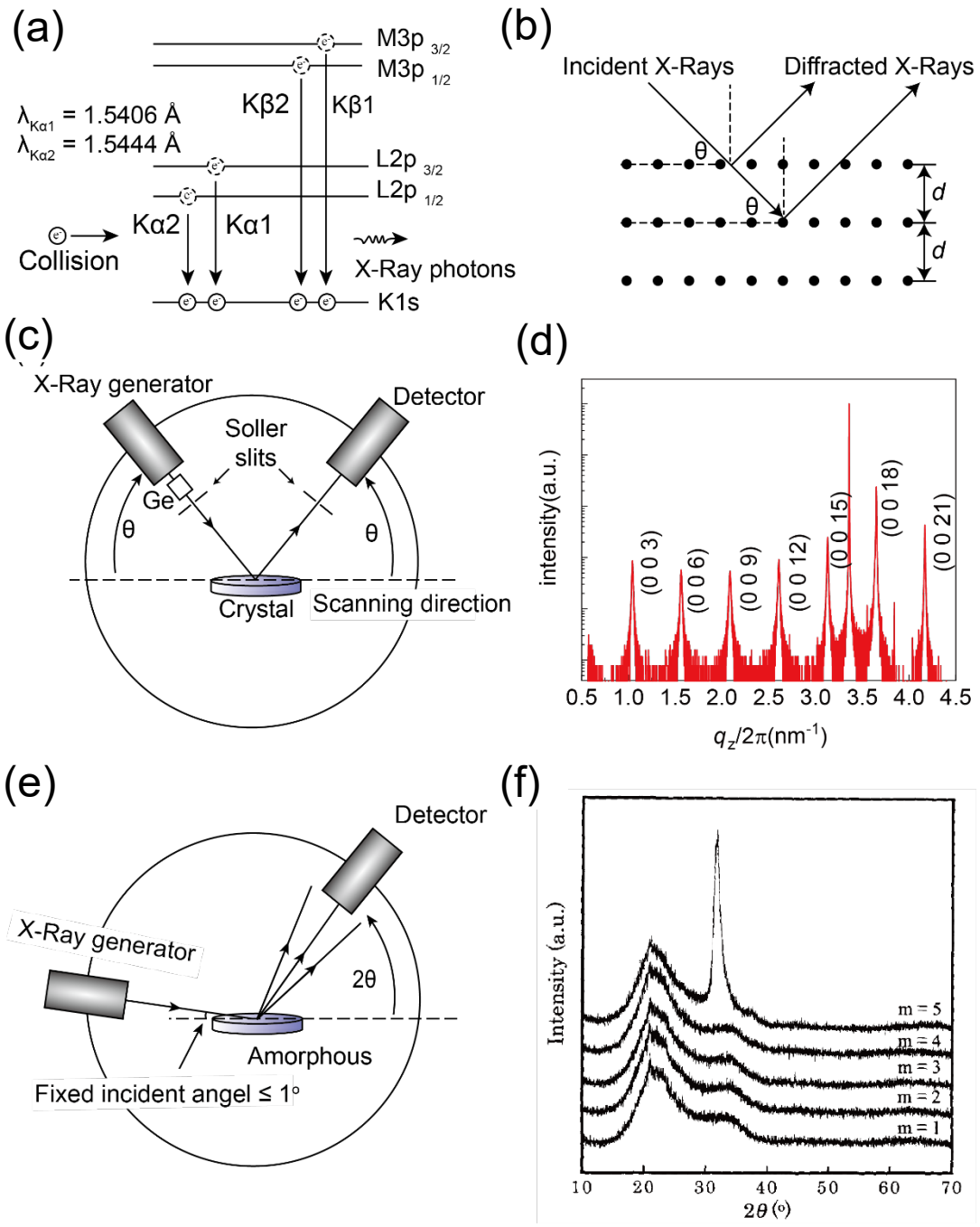

Figure 2 - 3 Schematic principle of XRD

(a) XRD generation (b) Bragg's law (c) Out of plan XRD ($\boldsymbol{\omega - 2\theta}$ scan) method. (d) Out of plan XRD pattern of $IGZO_m$ (e) GIXRD ($\boldsymbol{2\theta}$ scan with fixed $\boldsymbol{\omega}$) (f) GIXRD pattern of $IGZO_m$(m = 1-5) [4]

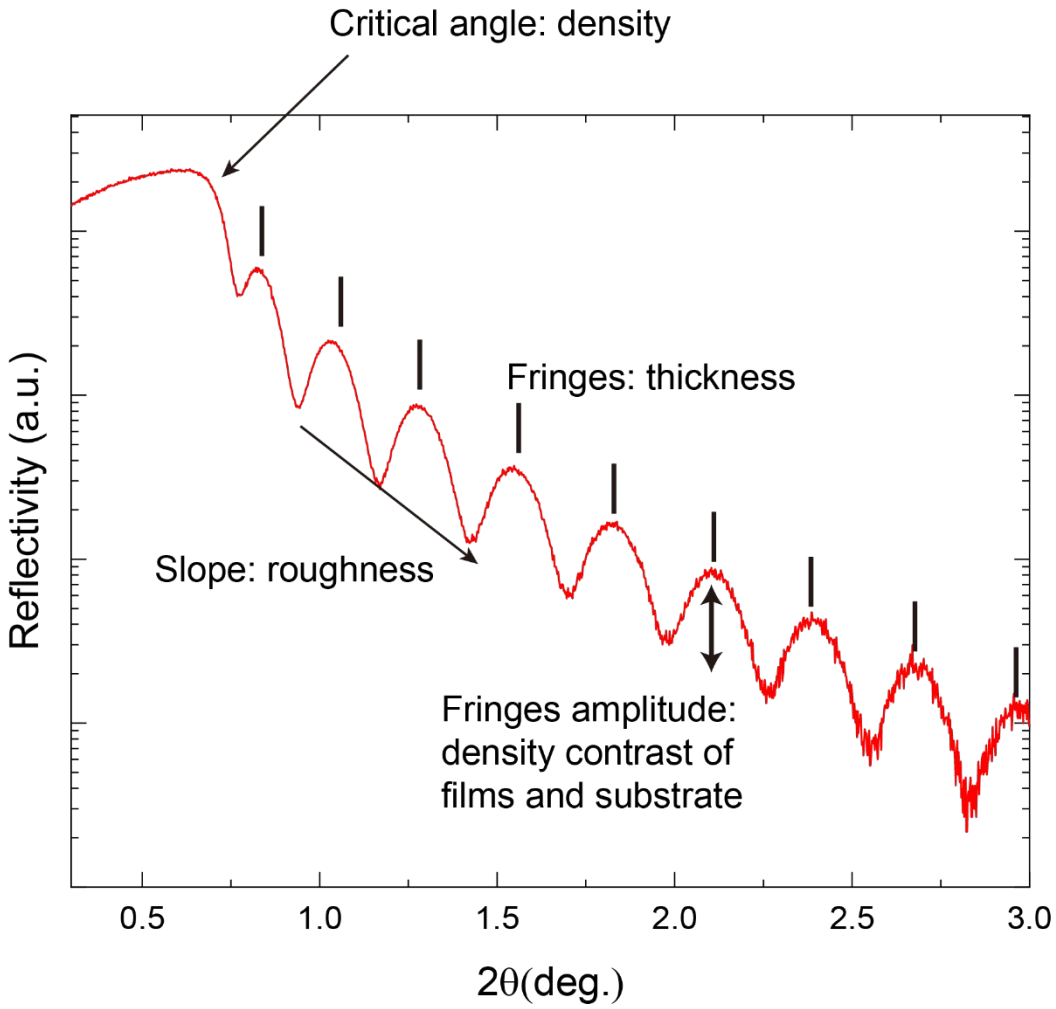

Figure 2 - 4 A example of X-ray reflectometry (XRR) pattern.

The XRR pattern measured from a-IZO ~ 30 nm with density of ~6.65 g/cm^3. Annotations in pattern indicate the types of features in a standard XRR analysis

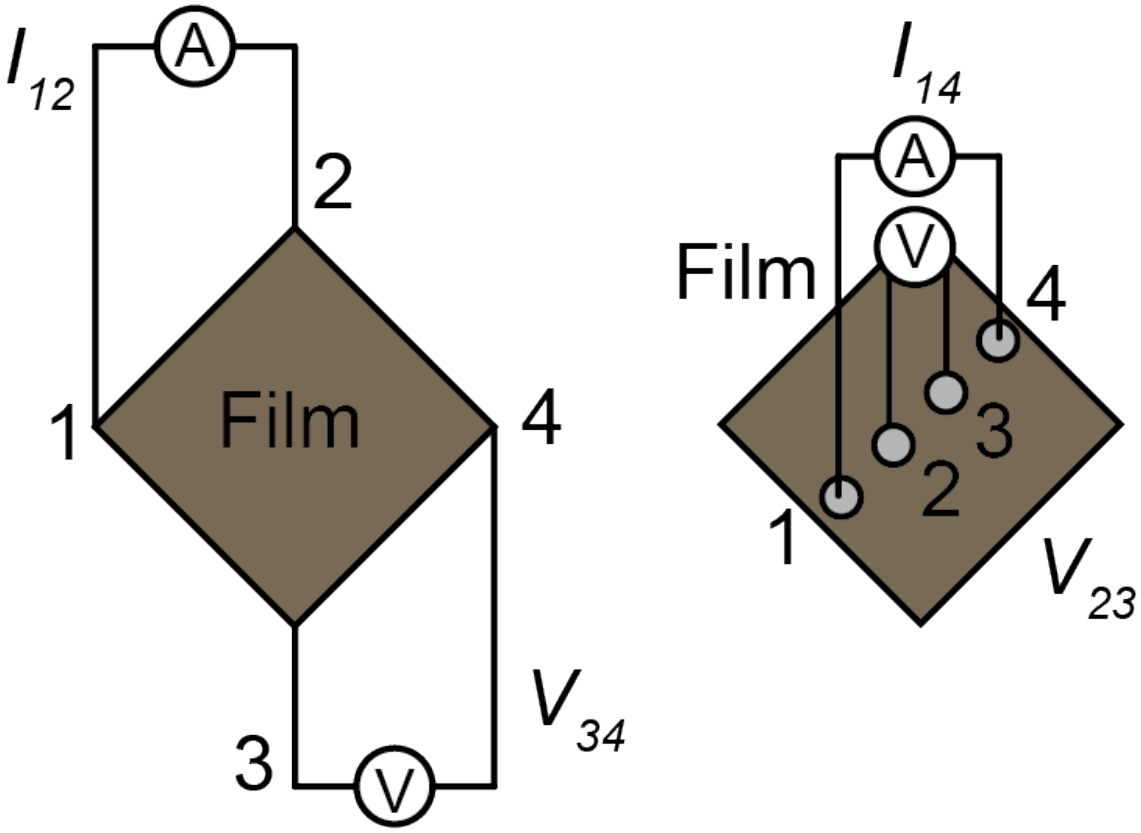

Figure 2 - 5 Schematic figure of Hall measurement

(a) Schematic figure of Van der Pauw method (b) Schematic figure of 4-point probe method

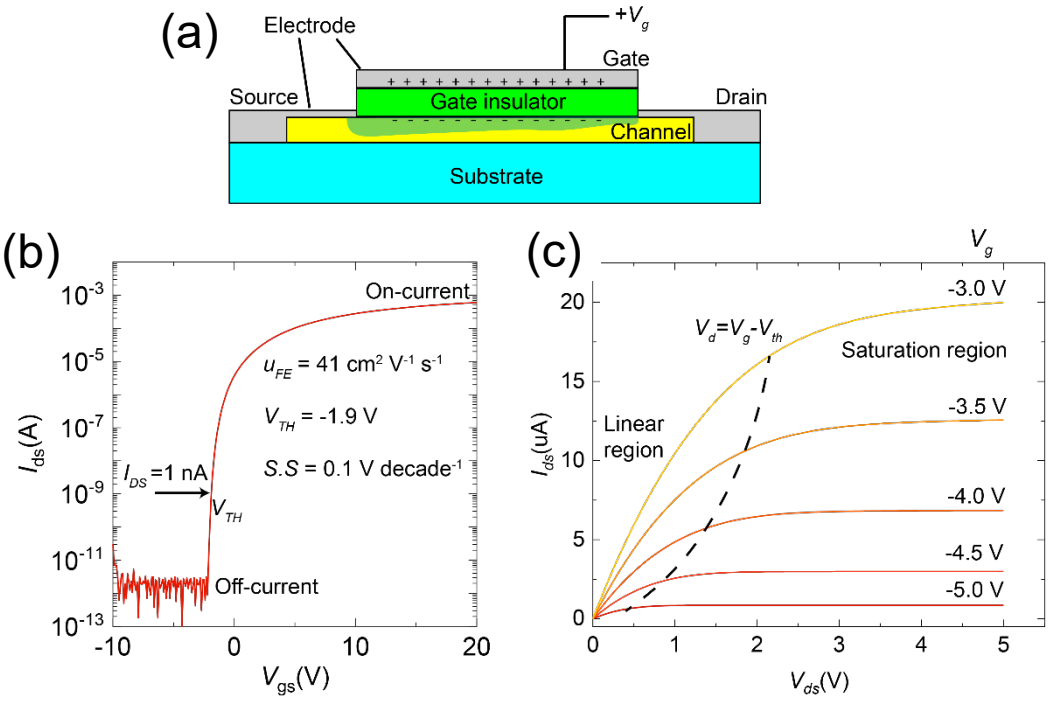

Figure 2 - 6 Schematic structure of an ideal TFT and figures of TFT characteristics

(a) Schematic figure of an ideal TFT structure with top gate. (b) Transfer curve of TFT. The annotations indicate the parameters which are able to extract. (c) Output characteristic of TFT, the linear and saturation region were separated with V_d.

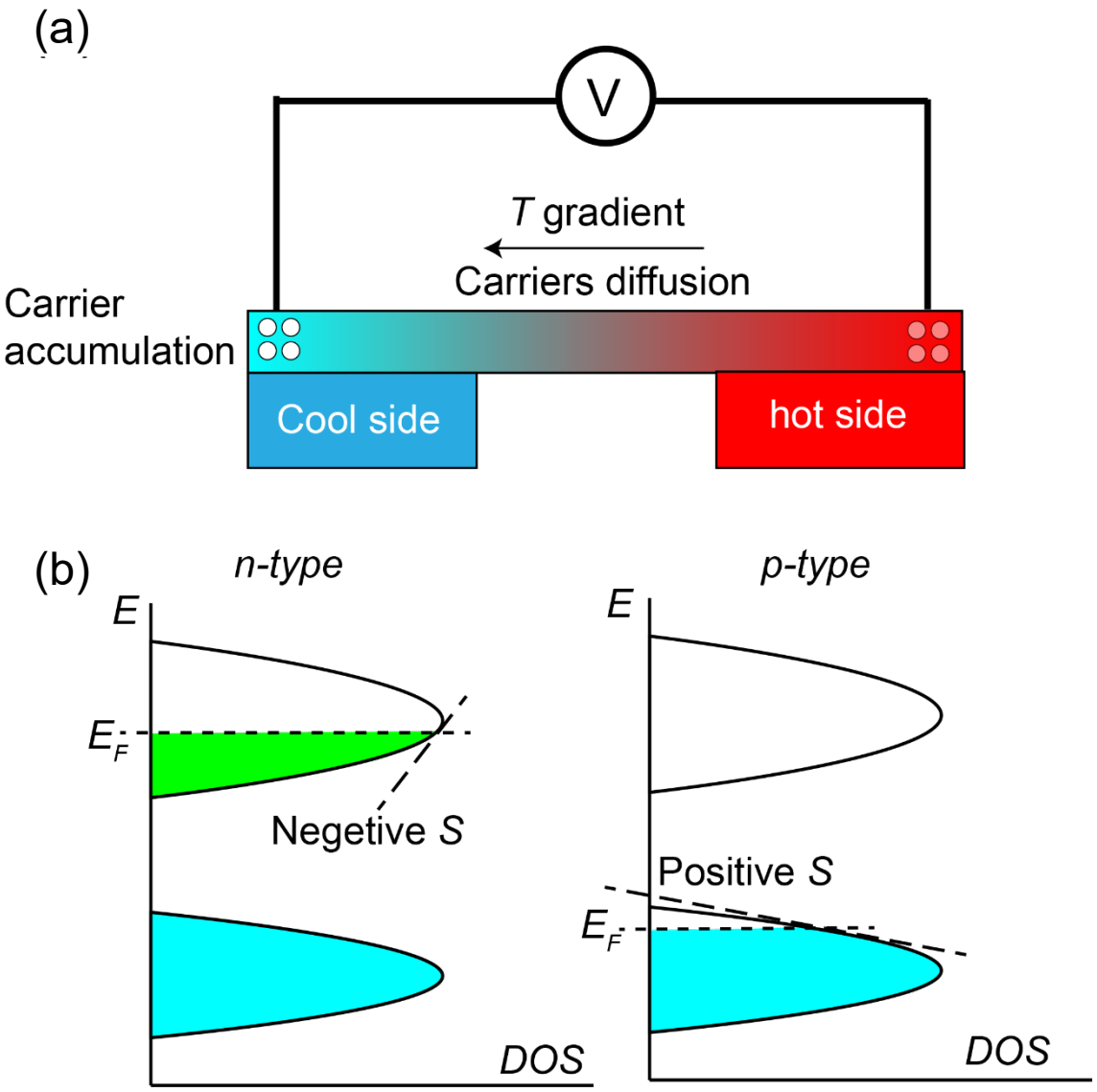

Figure 2 - 7 Schematic figure of thermopower measurement.

(a) Schematic figure of equipment setting (b) Relationship between *S* and type of charge carriers in semiconductor.

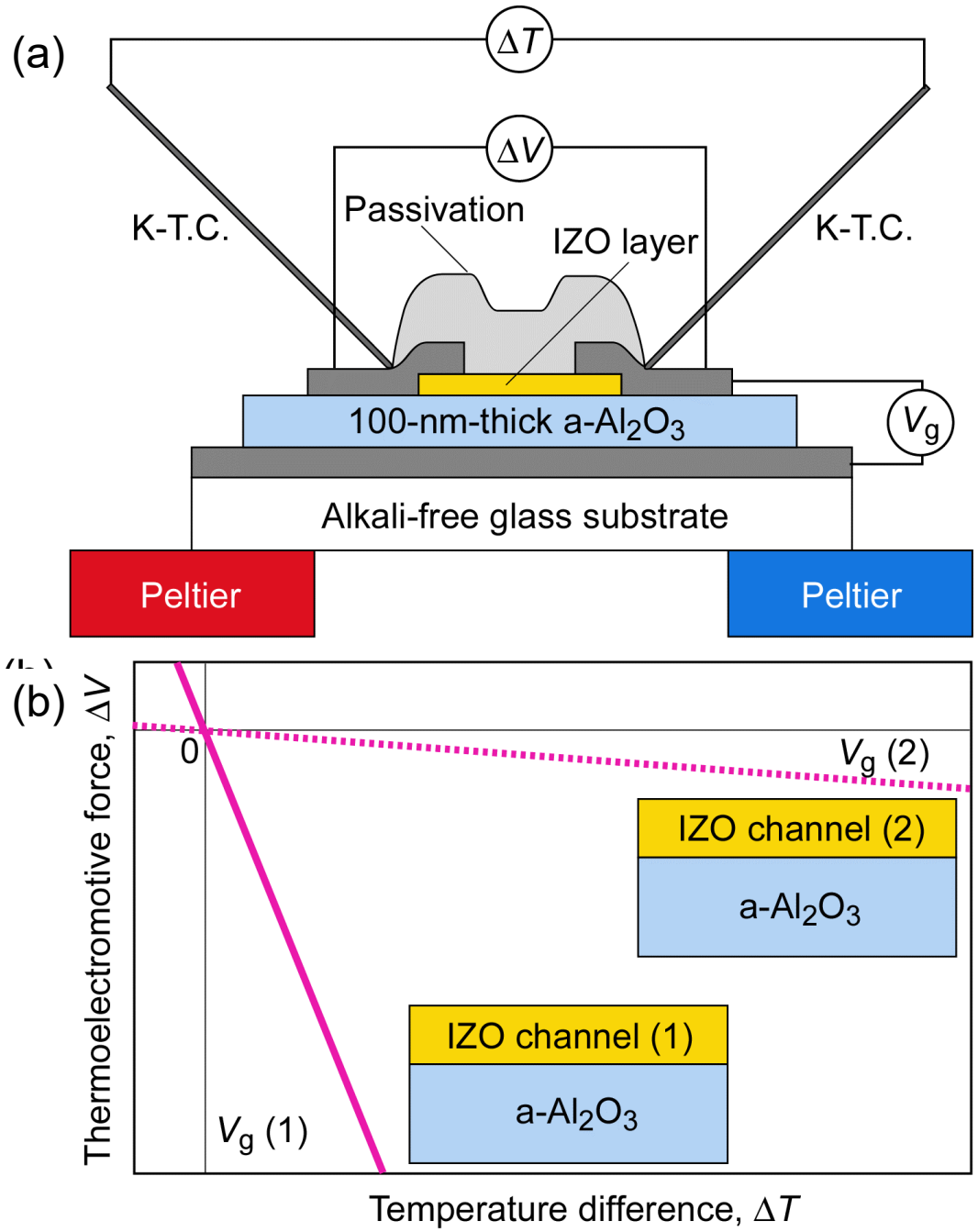

Figure 2 - 8 Schematic electric-field thermopower modulation method of the IZO TFTs.

(a) Schematic method of thermopower modulation (b) Schematic relationship between ΔT and ΔV of a TFT based on n-type semiconductor like In-Zn-O channel

Reference

[1] Eason, R. *Pulsed laser deposition of thin films: applications-led growth of functional materials*. John Wiley & Sons, (2007).

[2] Meyer, E. Atomic force microscopy. *Progress in surface science* **41**, 3-49 (1992).

[3] Bragg, W. H. & Bragg, W. L. The reflection of X-rays by crystals. *Proceedings of the Royal Society of London. Series A, Containing Papers of a Mathematical and Physical Character* **88**, 428-438 (1913).

[4] Orita, M., Ohta, H. *et al.* Amorphous transparent conductive oxide InGaO3 (ZnO) m (m≤ 4): a Zn4s conductor. *Philosophical magazine B* **81**, 501-515 (2001).

[5] Sanchela, A. V., Onozato, T. *et al.* Thermopower modulation clarification of the intrinsic effective mass in transparent oxide semiconductor $BaSnO_3$. *Phys. Rev. Mater.* **1**, 034603 (2017).

[6] Ohta, H., Kim, S. W. *et al.* High Thermoelectric Power Factor of High-Mobility 2D Electron Gas. *Adv. Sci.* **5**, 1700696 (2018).

[7] Sanchela, A. V., Wei, M. *et al.* Thermopower Modulation Clarification of the Operating Mechanism in Wide Bandgap $BaSnO_3$-$SrSnO_3$ Solid-Solution Based Thin Film Transistors. *Small* **15**, 1805394 (2019).

[8] Liang, D. D., Zhang, Y. Q. *et al.* Electric field thermopower modulation analyses of the

operation mechanism of transparent amorphous SnO_2 thin-film transistor. *Appl. Phys. Lett.* **116**, 143503 (2020).

[9] Yang, H., Zhang, Y. Q. *et al.* Thermopower Modulation Analyses of High-Mobility Transparent Amorphous Oxide Semiconductor Thin-Film Transistors. *Acs Appl Electron Ma* **4**, 5081-5086 (2022).

[10] Ghediya, P., Yang, H. *et al.* Improved Electron Transport Properties of Zn-Rich In-Ga-Zn-O Thin-Film Transistors. *J Phys Chem C* (2023).

Chapter 3. Anneal Temperature effect on structure and electron transport properties of Zn-incorporated In_2O_3 films

3.1 Object of this Chapter

In semiconductors, the carrier transport properties such as carrier concentration, mobility, resistivity, and field-effect mobility in TFTs were highly dependent on the structural characteristics of the specimen. For instance, scattering centers were introduced such as grain boundaries, as well as defects that disrupt the band structure, such as donor or acceptor levels induced by structural defects[1]. Commonly existed defects in IZO films include indium/zinc institution , interstitial In or Zn, oxygen vacancies[2]. The post-annealing process is widely used to suppress the defects in IZO films to enhance electron transport properties. However, the post-annealing process always promotes crystallization. Though $In_2O_3(ZnO)_m$ (where m is an integer) single crystals possess a complex layered structure, leading to crystallization become difficult to occur at lower annealing temperatures (e.g., <500 °C) [3-7], the uncertainty of annealing temperature effect on crystallinity is still a huge problem on proceed experiment on electron transport properties. Therefore, in order to determine the balance point of enhance electron transport properties and crystallization, an investigation of critical temperature of

crystallization is necessary.

In this chapter, a systematic study of the effect of annealing temperature on the crystallinity and electrical transport properties of IZO films were investigated. The results demonstrate that In-rich IZO films crystallize at 300°C, and the defects, such as oxygen vacancies contributing to carrier concentration, are effectively removed during this process. The results from this chapter will be used as a basement of the following experiment in this thesis.

3.2 Experimental

IZO Ceramic target of PLD preparation:

$In_2O_3(ZnO)_m$ with *Zn wt.%* = 10% and m = 1, 2, 3, 5, 7, 9, 20 ceramic target was prepared with conventional solid state reaction method. First In_2O_3 and ZnO powders within stoichiometric proportions was wet mixture with ethanol in mortar for 30 minutes and dried with heating lamp for 30 minutes. The dried mixed powder was pelletized and calcined at 1000ºC for 6h and then sintered at 1400 ºC. The surface of resultant pellets was polished to remove the top surface whose compositions with different stoichiometric proportion due to the Zn evaporation.

IZO film preparation

IZO films were fabricated on alkali-free glass substrates (EAGLE XG®, Corning®) by PLD method at 25 °C using a KrF excimer laser. The laser fluence during depositing was maintained as approximately 1.5 J/cm^{-2} with the frequency of 10 Hz. During deposition, the PLD chamber was evacuated to a base pressure of 1.0×10^{-3} Pa, and the oxygen partial pressure was maintained to approximately 3 Pa. All films were annealed in Muffle furnace in air with various temperature from 100 ºC to 300 ºC.

Because of the Zn easily evaporation during depositing, the ZnO weight ratio (*Zn w.t.%*) of resultant film always slightly shifts from that of target. With the assumption that the Zn evaporation was independent of Zn concentrations in target, the gradient of *Zn w.t.%* in resultant films was regarded as same as those of ceramic target in this chapter. The *Zn w.t.%* of resultant films were roughly denoted by ZnO weight ratio as same as target:

$$Zn\ w.t.\% = \frac{m(ZnO)}{m(ZnO) + m(In_2O_3)}$$

where *m* is mass.

Structure characterization

The thickness, density, and surface roughness of the resultant IZO films were measured using X-ray reflectivity (XRR, ATX-G, Rigaku Co.). The crystallinity was characterized by GIXRD. The incident angle of the X-rays was fixed at 1° during GIXRD measurement.

Electron transport properties

The electric transport properties containing ρ, n, and μ_{Hall} were measured by a DC four-probe method with a van der Pauw electrode configuration. S was measured using a conventional steady-state method at 25 °C with laboratory-made equipment. The temperature gradient was generated with a pair of Peltier devices under the films as **Figure 2 - 7 a**. The cool side and hot side were on the 2 opposite edges of sample to create temperature gradient while performing Voltage measurement.

3.3 Results and discussion

Figure 3 - 1 presents the GIXRD patterns of (a) as deposited and (b) annealed at 300°C IZO films with thickness of 100 nm ~30 nm IZO films. The Zn concentrations range from 10 to 67 *Zn wt.%*, corresponding to target that 10 *wt.%* Zn and m values of 1, 2, 3, 5, 7 respectively. For both thicknesses and *Zn wt.%*, the as-deposited films exhibit an amorphous phase. After annealing at 300°C, the 100 nm films with *Zn wt.%* = 10% crystallized as separate phase that In_2O_3 (circle) and IZO (triangle), while the 30 nm films with the same Zn content remained amorphous. This result indicates that thinner thickness of IZO films contribute to suppress crystallization probably due to reduced bulk volume,

which likely suppress nucleation during thermal treatment[8].

To determine the optimal annealing temperature for crystallization while enhancing electric properties by effectively reducing oxygen vacancies, electron transport properties and crystallinity were analyzed at annealing temperatures ranging from 100°C to 300°C with 100°C step. **Figure 3 - 2** shows the GIXRD patterns of 30 nm IZO films with *Zn wt.%* = 0%, 10%, 23%, 37%, 73%, and 85%. Across all compositions of *Zn wt.%* > 0 annealed ≤200°C, the halo peak at ~ 32° was observed indicating the amorphous IZO phase. At 300°C, the In_2O_3 peak at 30.6° and a halo peak at 32° were observed in In-rich compositions (*Zn wt.%* = 10%), suggesting the phase separation of crystalized In_2O_3 phase and amorphous IZO phase. Notably, In_2O_3(*Zn wt.%* = 0 %) films crystalized when annealing temperature ⩾ 100°C. These results indicate a strong dependence of crystallization of IZO behavior on Zn concentration and annealing temperature, which is attributed to the reduced network connectivity in In-rich compositions, which lowers the energy barrier for crystallization at elevated temperatures [9-11].

Figure 3 - 3 examines the influence of annealing temperature on the electrical transport properties of IZO films. For $T \leq 100$∘C, the mobility and carrier concentration of all IZO films remained similar to those of as-deposited values, indicating that the energy was insufficient to activate the recovery of oxygen vacancies. At T = 200°C, μ_{Hall} increased

and *n* abnormal decreased compared to the as-deposited state, suggesting partial recovery of oxygen vacancies and the ionic scattering with oxygen vacancies is one of the dominant factors of electron transportation. The observed decrease in carrier concentration with increasing *Zn wt.%* (*Zn wt.%* > 0) is consistent with trends in oxide semiconductors, where Zn incorporation reduces carrier density due to its lower orbital overlap with neighboring atoms compared to In[2,7,12].

At 300°C, both carrier concentration and Hall mobility decreased significantly compared to the as-deposited state and exhibited even lower values ~ 10^{17} than at 200°C for most *Zn wt.%*, indicating a more effective suppression of oxygen vacancies. This value is lower than the commonly reported magnitude of ~ 10^{20}. Notably, the IZO film with *Zn wt.%* = 10% exhibited relative higher *n* and lower u_{FE} comparing with a-IZO, which could be attributed to grain boundaries. This phenomenon will be detailed discussed in Chapter 4. An exception was observed for *Zn wt.%* = 85%, where the carrier concentrations remained comparable between the 200°C and 300°C annealed states, suggesting that oxygen vacancies were already fully recovered at 200°C.

Interestingly, the *n* demonstrated a non-monotonic trend with *Zn wt.%*, initially decreasing and then increasing to higher *Zn w.t.%*. This behavior, independent of Hall mobility, implies that while oxygen vacancies which major contributors to carrier

generation were substantially suppressed, additional defect states caused by Zn incorporation might have contributed to the observed increase in carrier concentration at higher Zn levels. The trend of thermopower vs *Zn wt.%* is opposite with *n* vs *Zn w.t%*, clarified the independence relationship between intrinsic degenerate behavior of semiconductor IZO and annealing temperature.

3.4 Conclusion

In the chapter, I investigated the structural and electrical transport properties of IZO films with varying *Zn w.t.%* under different annealing conditions. GIXRD results showed that as-deposited films were amorphous across all *Zn w.t.%* and thicknesses, while crystallization after annealing at 300°C only occurs in 100 nm films with *Zn w.t.%* = 10% and 0%, 30 nm *Zn w.t.%* = 0%, indicating thinner films (~30 nm) suppressed crystallization due to enhanced surface energy and reduced bulk volume. The annealing temperature significantly influenced electron transport properties: at 200°C, partial recovery of oxygen vacancies decreased carrier concentration and Hall mobility, while at 300°C, oxygen vacancies were more effectively suppressed, except at high Zn concentrations (e.g., *Zn wt.%* = 85%), where defect states possibly contributed to

increased carrier density.

These results demonstrate film thickness, and annealing conditions in modulating structural and electrical properties. Precise control over these parameters is essential for optimizing IZO films in applications.

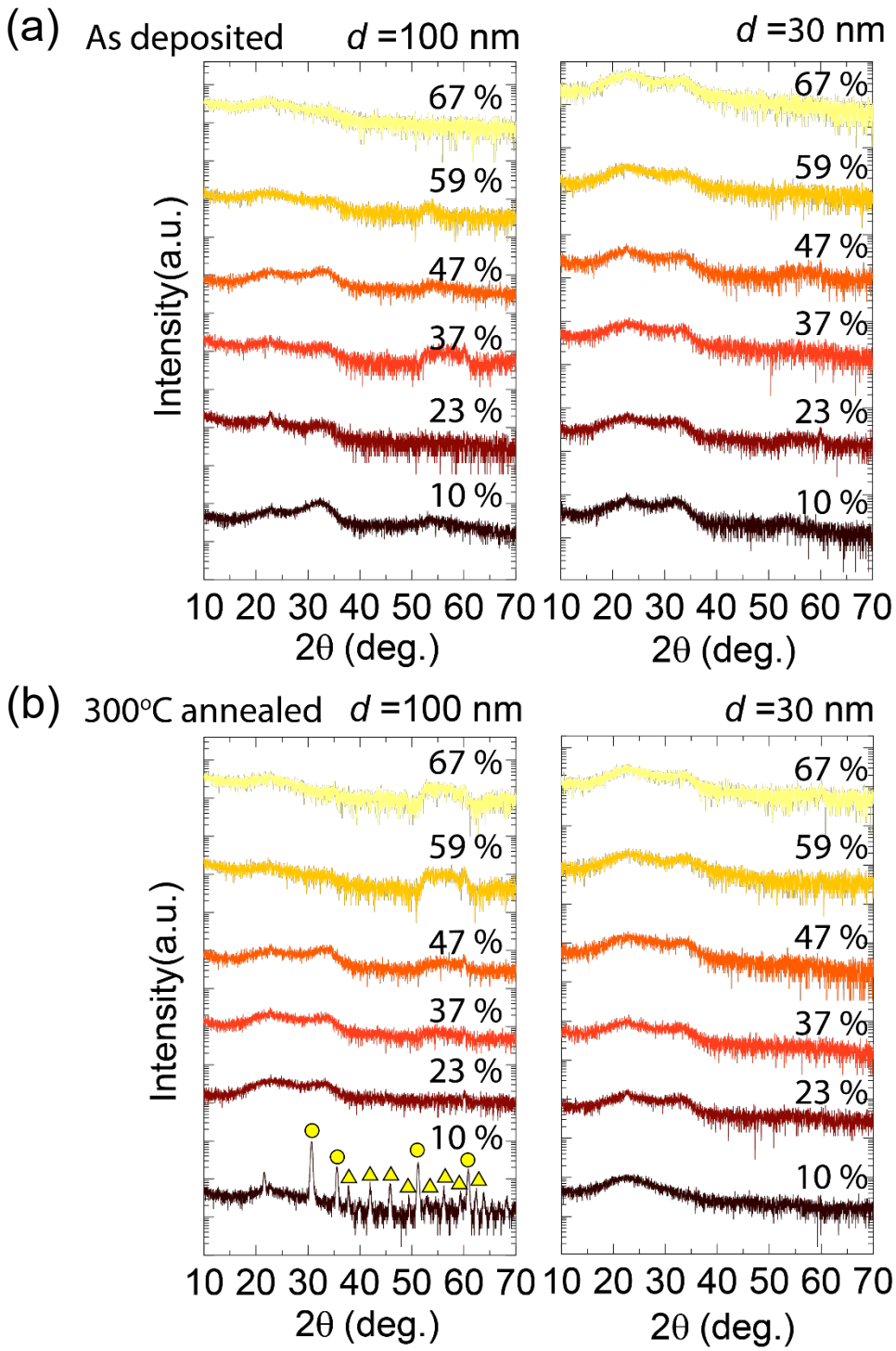

Figure 3 - 1 GIXRD patterns of IZO films with different thickness

(a) as deposited films (b) 300°C annealed films

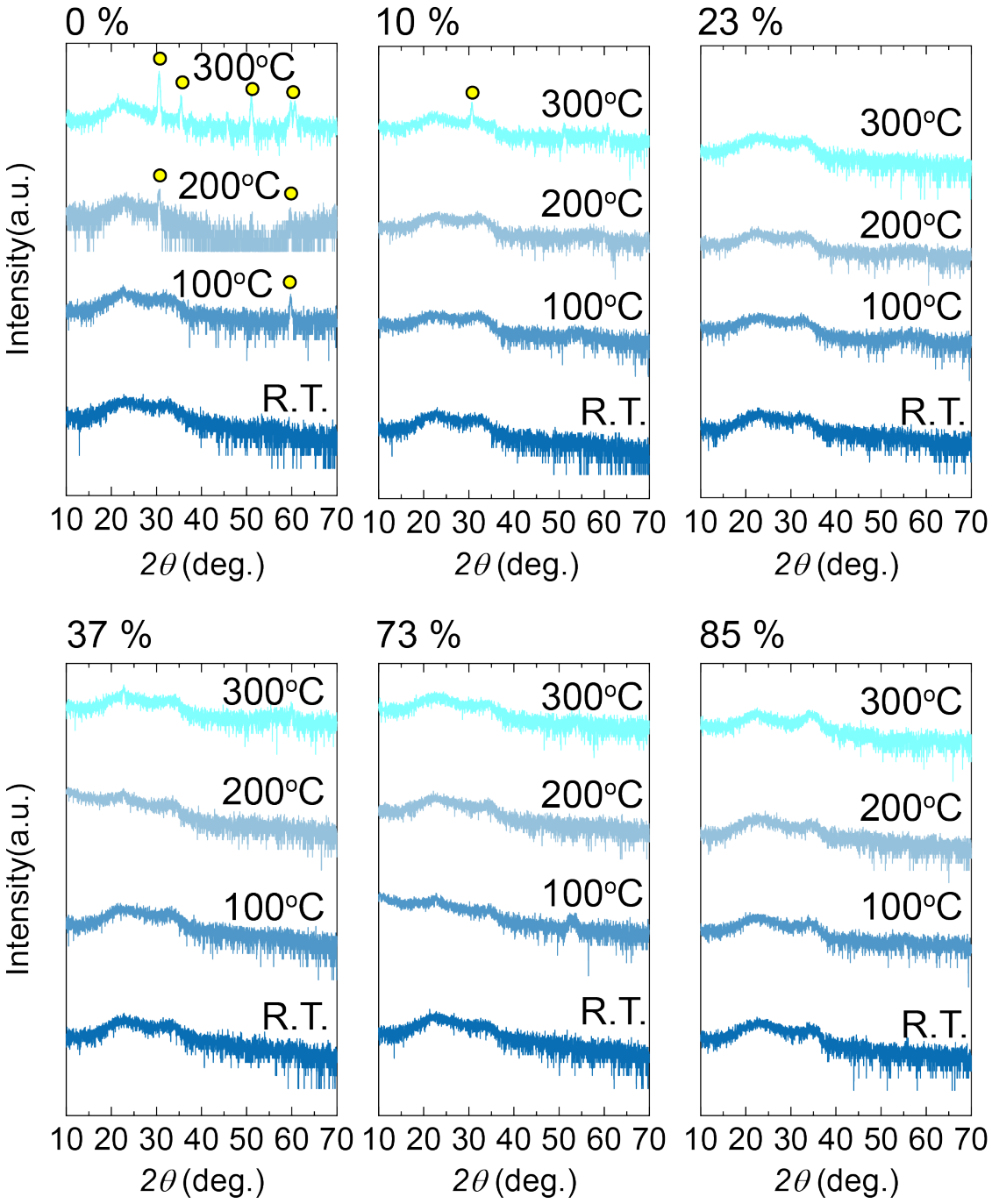

Figure 3 - 2 GIXRD of *Zn wt.%* (0% - 85%) IZO films annealed at various temperature.

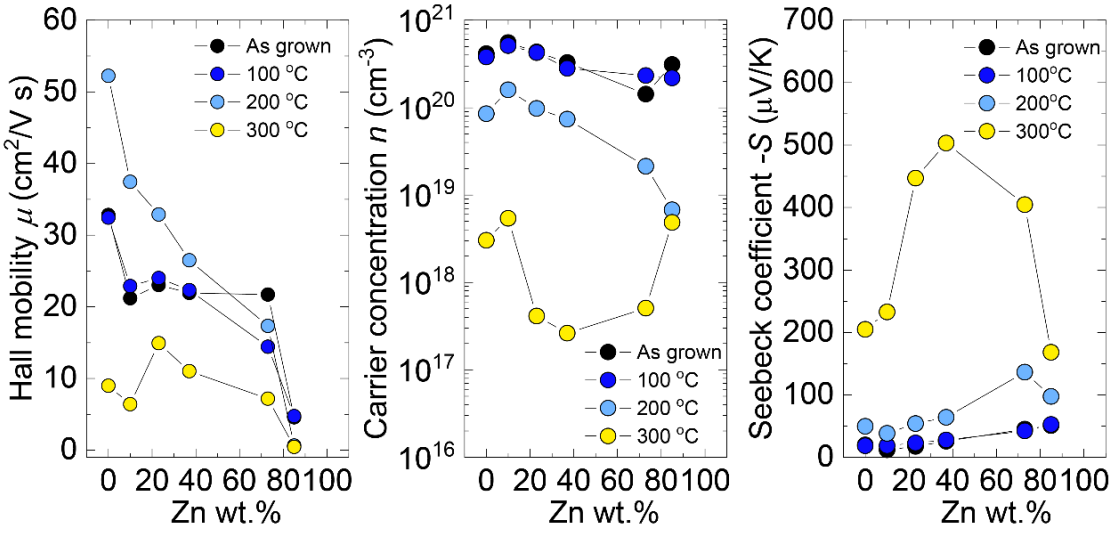

Figure 3 - 3 Relationship between electric transport properties and annealing temperature in IZO films.

Reference

[1] Sze, S. M., Li, Y. *et al. Physics of semiconductor devices*. John wiley & sons, (2021).

[2] Ito, N., Sato, Y. *et al.* Electrical and optical properties of amorphous indium zinc oxide films. *Thin solid films* **496**, 99-103 (2006).

[3] Barquinha, P., Goncalves, G. *et al.* Effect of annealing temperature on the properties of IZO films and IZO based transparent TFTs. *Thin Solid Films* **515**, 8450-8454 (2007).

[4] Lee, C., Lee, W. *et al.* Influence of annealing atmosphere on the structure, resistivity and transmittance of InZnO thin films. *Ceramics international* **34**, 1089-1092 (2008).

[5] Yaglioglu, B., Yeom, H.-Y. *et al.* Crystallization of amorphous In2O3–10 wt% ZnO thin films annealed in air. *Applied Physics Letters* **86** (2005).

[6] Nomura, K., Ohta, H. *et al.* Room-temperature fabrication of transparent flexible thin-film transistors using amorphous oxide semiconductors. *nature* **432**, 488-492 (2004).

[7] Nomura, K., Takagi, A. *et al.* Amorphous oxide semiconductors for high-performance flexible thin-film transistors. *Japanese journal of applied physics* **45**, 4303 (2006).

[8] Trofimov, V. I., Trofimov, I. V. *et al.* The effect of finite film thickness on the crystallization kinetics of amorphous film and microstructure of crystallized film. *Thin Solid Films* **495**, 398-403 (2006).

[9] Utsuno, F., Inoue, H. *et al.* A structural study of amorphous In2O3–ZnO films by grazing incidence X-ray scattering (GIXS) with synchrotron radiation. *Thin Solid Films* **516**, 5818-5821 (2008).

[10] Kamiya, T., Nomura, K. *et al.* Origins of high mobility and low operation voltage of amorphous oxide TFTs: Electronic structure, electron transport, defects and doping. *Journal of display Technology* **5**, 273-288 (2009).

[11] Utsuno, F., Inoue, H. *et al.* Structural study of amorphous In2O3 film by grazing incidence X-ray scattering (GIXS) with synchrotron radiation. *Thin solid films* **496**, 95-98 (2006).

[12] Kamiya, T. & Hosono, H. Material characteristics and applications of transparent amorphous oxide semiconductors. *NPG Asia Materials* **2**, 15-22 (2010).

Chapter 4 Stabilization of Zn-incorporated In_2O_3 Thin-Film Transistor

4.1 Object of this Chapter

As mentioned in Chapter 1, with the increasing demand for higher-definition displays operating at high frequencies (e.g., 480 Hz, single scan), thin-film transistors (TFTs) with higher field-effect mobility (μ_{FE} > 50 $cm^2\ V^{-1}\ s^{-1}$) are essential for driving pixel circuits.[1-4] Among various reports on thin oxide semiconductor (TOS) TFTs achieving μ_{FE} values above 50 $cm^2\ V^{-1}\ s^{-1}$, indium oxide (In_2O_3)-based TFTs have emerged as promising candidates due to their exceptional field-effect mobility, often exceeding 100 $cm^2\ V^{-1}\ s^{-1}$.[5] However, these devices suffer from significant drawbacks, particularly their poor reliability under negative gate bias stress, attributed to the adsorption and/or desorption of gas molecules at grain boundaries.[5,6]

In Chapter 3, I initially discussed about the incorporation of zinc (Zn) into In_2O_3 effect on crystallization and electric properties, which aligns with existing literature and helps mitigate issues related to grain boundary defects by stabilizing an amorphous phase.[7-15] Such a structural and electric properties adjustment is crucial for ensuring the performance of In_2O_3-based TFTs for industrial applications and it is the basement for

experiment in Chapter 4.

This chapter presents a systematic investigation of the electrical transport properties of zinc-incorporated In_2O_3 (IZO) films and TFT across a wide range of *Zn a.t.%* (9%–86%) and discuss about the effect on how Zn content influences the crystallinity and the subsequent impact on carrier transport properties and stability in TFT.

The results reveal that the crystallization of IZO films is effectively suppressed when the *Zn a.t.%* = 25% - 68%, while crystallizing when *Zn a.t.%* $\geqslant$ 86% and $\leqslant$ 9%. Specifically, amorphous IZO-TFTs with 25% Zn demonstrated the highest μ_{FE} of 41 $cm^2 V^{-1} s^{-1}$, along with excellent reliability. In contrast, polycrystalline IZO-TFTs exhibited significantly lower μ_{FE} values (<12 $cm^2 V^{-1} s^{-1}$) due to the formation of grain boundaries, which also contributed to poor stability under positive gate bias stress due to electron trapping at the polycrystalline/insulator interface.

4.2 Experiment

Fabrication of IZO films

In this experiment, IZO films and TFT device were fabricated with ceramic target with various Zn ratio (10 wt.% ZnO added In_2O_3, $In_2O_3(ZnO)_m$ and m = 1, 2, 9, and 20) which were prepared using a conventional ceramic process.

IZO films were fabricated on alkali-free glass substrates (EAGLE XG®, Corning®) by PLD at 25 °C using a KrF excimer laser (~1.5 J cm^{-2} $pulse^{-1}$, 10 Hz). In order to suppress the defects like oxygen vacancies, which highly affect the mobility and carrier concentraions, the oxygen pressure was maintained at 3 Pa during deposition. Typical deposition rate was ~0.3 nm s^{-1}.

Since the resultant IZO film is easily separated into several phases (e.g. m = 3 in target, and m = 1 and 2 in resultant films), the certain concentration of Zn was measured using inductively coupled plasma mass spectrometry (ICP-MS). The concentration of Zn was denoted as *Zn a.t.%* and was defined with following equation:

$$Zn\ a.t.\% = \frac{Zn}{In + Zn} \times 100(\%)$$

The *Zn a.t.%* of resultant films were 9%, 25%, 41%, 68%, and 86% respectively correspond to *Zn w.t.%* in target with ascending arrangement. In order to suppress the n which probably induced from oxygen vacancies after the deposition, the IZO films were annealed at 300 °C in air for 0.5 h.

Surface morphology observation, structure analysis and electron transport properties of the IZO films

The surface morphology was observed with AFM (Nanocute, Hitachi Co. AFM). The thickness, density, and surface roughness of the resultant IZO films were measured using

XRR (ATX-G, Rigaku Co.). The GIXRD patterns clarify the crystallinity of IZO films. The ρ, n, and μ_{Hall} of the IZO thin films were measured by a DC four-probe method with a van der Pauw electrode configuration. S was measured using a conventional steady-state method at 25 °C with laboratory-made equipment.

Fabrication of IZO-TFTs

Indium Zinc Oxide (IZO) thin-film transistors (TFTs) of the bottom-gate, top-contact configuration was fabricated on alkaline-free glass substrates (EAGLE XG®, Corning®), as illustrated in **Figure 4 - 1**.

Firstly, a 100-nm-thick aluminum oxide (AlO_x) layer as the gate insulator was deposited directly onto the ITO-coated glass substrate using atomic layer deposition (ALD), a method known for its excellent film uniformity and precise thickness control to ensure high-quality AlO_x. The dielectric permittivity ε_r and a capacitance per unit area C_i of the AlO_x were 8 and 70 nF cm^{-2} respectively.

Since oxide tend to crystallize in thicker sample and thinner IZO films exhibited high mobility[16], a thin film with 5-nm-thick rather than 30 nm IZO (*Zn a.t.%* = 0% - 86%) films were deposited on the AlO_x layers using pulsed laser deposition (PLD) at room temperature under an oxygen partial pressure of 3 Pa. A stencil mask was employed during this step to define the active layer geometry precisely. After the deposition of the

IZO active layer, the multilayer stack was annealed in ambient air at 300 °C for 0.5 hours. This thermal treatment aimed to reduce defects such as oxygen vacancies, which are critical for tuning the electrical properties of IZO.

Following the annealing, 100-nm-thick ITO films were deposited using PLD on the multiple layered structure as the source and drain electrodes. During deposited, another stencil mask was employed to ensure the geometric relationship. The resulting *L* and *W* were 200 μm and 400 μm, respectively, ensuring adequate dimensions for reliable electrical measurements. Then, the Y_2O_3 passivation layer was selected for its excellent chemical stability and ability to protect the TFT channel from environmental degradation. A ~50-nm-thick yttrium oxide (Y_2O_3) film was deposited using PLD through the 3rd type of stencil mask for device passivation.

Finally, the entire device underwent a second thermal annealing process at 300 °C in air for 0.5 hours. This post-deposition annealing step further improved the interface quality between the layers and reduced residual defects, enhancing overall device performance.

4.3 Results and discussion

Figure 4 - 2 shows the GIXRD patterns of the (a) as deposited and (b) 300 °C annealed In_2O_3 (*Zn a.t.%* = 0%) and IZO (*Zn a.t.%* = 9%, 25%, 41%, 68%, and 86%) films. As

same as the results exhibited in Chapter 3, the In_2O_3 films exhibited intense diffraction peaks intendent with annealing process, indicating their polycrystalline nature. This result is also consistent with previous reports in which In_2O_3 was crystallized at room temperature.[5] For annealed IZO films, Zn concentrations range from 25%−68%, the GIXRD pattern contains a broad halo centered at approximately $2\theta \sim 34^{o}$ for which is characteristic of amorphous structure. As well, the diffraction peaks appear for Zn concentrations of 9% and 86%, which exhibited polycrystalline nature. On the contrast, the IZO films with low (<25%) and high Zn (>68%) concentrations crystallized after annealed under 300°C. These results indicate a moderate amount of Zn in IZO films (*Zn a.t.%*: 25%−68%) stabilizes the amorphous structure after annealing at 300 °C. In Zn-rich area, it should be noticed that though 68% Zn is higher than reported *Zn at. %* of polycrystalline IZO (50 *at. %*)[17], films still stay in amorphous phase. In In-rich area, the Zn ratio of 9% Zn films is well consistent with the reported crystallization of Zn ratio < 16 *wt.%*[18,19]. **Figure 4 - 3** show the AFM pattern of polycrystalline (9% and 86%) and amorphous (25%) IZO films. The IZO with 9% and 86% *Zn a.t.%* exhibited higher root mean square (RMS) of 0.8 nm and 0.9 nm which is almost 3 times of those of *Zn a.t.%* = 25% films, suggesting polycrystalline IZO film exhibit a rougher surface.

Figure 4 - 4 illustrates the n, μ_{Hall}, and S as functions of Zn concentration in IZO films.

For the as-deposited IZO films, *n* is initially high that on the order of 10^{20} cm^{-3} and shows a slight decrease with increasing Zn concentration. However, after annealing, *n* decreases significantly to approximately 10^{17} cm^{-3} **(Figure 4 - 4 a)**. This marked reduction can be attributed to the substantial suppression of oxygen vacancies within the amorphous IZO films upon annealing. In contrast, the *n* values of polycrystalline In_2O_3 and the 9% Zn IZO film exhibit only minor reductions post-annealing, which may be explained by the adsorption of O^{2-} or OH^- ions at grain boundaries. This adsorption leads to the formation of a double Schottky barrier, rather than filling deficiencies like oxygen vacancies.[20]

The μ_{Hall} of as-deposited films, regardless of Zn concentration, is observed in the range of 20–30 $cm^2\,V^{-1}\,s^{-1}$(**Figure 4 - 4 b**). After annealing at 300 °C, the In_2O_3 film demonstrates the highest μ_{Hall} value, reaching 22.2 $cm^2\,V^{-1}\,s^{-1}$. Generally, grain boundaries have a relatively limited effect on μ_{Hall} in transparent conductive oxides with high carrier concentrations ($n > 10^{19}$ cm^{-3}), as electrons can effectively tunnel through the narrow barriers.[21] However, for the 9% Zn film, μ_{Hall} drops significantly to 6.4 $cm^2\,V^{-1}\,s^{-1}$ after annealing, which is likely due to increased grain boundary scattering caused by the reduced *n*.

The μ_{Hall} of the amorphous IZO films gradually decreases after annealing as the Zn concentration increases. To gain deeper insight into the carrier transport properties, I

measured the Seebeck coefficient *S* of the IZO films **(Figure 4 - 4 c)**. As mentioned in Chapter 2.6, unlike electron mobility, *S* is a factor less dependent with the parameter coupled with film quality such grain boundaries, making it a valuable parameter for analyzing intrinsic carrier transport behavior such as carrier effective mass m^*[22-24]. The absolute value of S for the as-deposited films is relatively small (<50 μV K^{-1}), consistent with their high carrier concentrations. Following annealing, S increases significantly (>400 μV K^{-1}) in the amorphous IZO films, reflecting their substantially reduced carrier concentration (~10^{17} cm^{-3}).

Figure 4 - 5 illustrates the thermopower *S* of the IZO films across varying Zn concentrations. Since the mobility is inversely proportional to effective mass m^* as following equation:

$$\mu = \frac{e\tau}{m^*}$$

where *e* is the electron charge and τ is the carrier relaxation time, the carrier transport properties can be inferred from thermopower measurements. **Figure 4 - 5 a** present the *S* values of the IZO films as a function of *n* on a logarithmic scale at room temperature. The measured *S* values align well with the calculated trends corresponding to m^* in the range of 0.1−0.2 m_0 (the free electron mass), regardless of Zn concentration. For the IZO film with 86% Zn, however, *S* is lower than the simulated value in the linear correlation region.

This abnormal behavior likely arises from non-parabolicity-induced tail states situated just below the conduction band edge (**Figure 4 - 5 b**).

The obtained m^* values (0.1−0.2 m_0) for the amorphous IZO films are consistent with previously reported m^* values for IZO ($m_d^*/2 = 0.15\, m_0$), indicating that $m*$ remains largely unaffected by Zn concentration.[25,26] This observation suggests that the Zn 4s-orbital-dominated conduction band bottom retains a similar band dispersion to the In 5s-orbital-dominated conduction band bottom[27], which could be attributed to the dominance of the In 5s orbitals in forming the conduction band and the relatively minor role of Zn orbitals. Consequently, the incorporation of Zn into In_2O_3 films stabilizes the amorphous structure without introducing additional carrier scattering centers.

Subsequently, I fabricated IZO TFTs with various Zn concentrations and measured their transistor characteristics.

Figure 4 - 6 a present the transfer characteristics of IZO TFTs measured at room temperature. The devices were configured with a L of 200 μm and a W of 400 μm. The *S.S.* and V_{TH} values corresponding with *Zn a.t.%* are summarized in **Table 1**. Notably, the threshold voltage gradually shifted positively as the Zn concentration increased, which can be attributed to a reduction in the electron concentration n within the IZO channel layer.

Figure 4 - 6 c illustrates the output characteristics for IZO TFTs with a *Zn a.t.%* equal to 25%. The drain current I_{ds} exhibits clear pinch-off behavior along with current saturation at higher V_{ds}, clarifying the TFT work in saturation region. Therefore, a drain voltage V_{ds} of +5 V was applied across all experiments to ensure TFT works in saturation region. The μ_{FE} was determined from the equation derived from saturation regime as following, which was also mentioned in Chapter 2.4.[28]

$$\mu_{FE} = \frac{\left(d\sqrt{I_d}/dV_g\right)^2}{(W/2L)C_i},$$

Figure 4 - 6 b shows the variation of μ_{FE} as a function of Zn concentration, with the values extracted from **Figure 4 - 6 d**. The observed trend reveals that amorphous IZO TFTs exhibit higher μ_{FE} compared to their polycrystalline counterparts. This improvement is primarily due to the absence of grain boundary scattering in the amorphous phase. The μ_{FE} decreases monotonically with increasing Zn concentration, consistent well with the trend observed in the μ_{Hall} shown in **Figure 4 - 4 b**. The optimal device performance was achieved for the amorphous IZO TFT with a Zn concentration of 25%, which exhibited μ_{FE} = 41 $cm^2\ V^{-1}\ s^{-1}$, a *S.S.* of 0.10 V dec^{-1}, and a V_{th} of −1.9 V.

Figure 4 - 7 exhibit the transfer curves with PBS and NBS, showing the variations in the transfer characteristics under PBS and NBS conditions. The duration of bias stress

applied in both NBS and PBS experiment was up to 5000 seconds treating at room temperature in air. **Figure 4 - 8** summarizes the stability results of IZO TFTs under NBS and PBS conditions, which exhibit the threshold voltage V_{th} shifts observed after 5000 seconds of PBS (**Figure 4 - 8 a**) and NBS (**Figure 4 - 8 b**) treatment for different *Zn a.t.%*.

It is worth noting that the effective stress voltage ($V_{GS}-V_{th}$) applied to the channel was not constant due to variations in V_{th} with *Zn a.t.%* (**Table 2**). However, no significant correlation was found between the effective stress voltage and the observed V_{th} shifts. Under NBS conditions, the V_{th} shifts remained minimal, less than 0.3 V, regardless of Zn concentration or the crystalline phase. This stability is attributed to the role of gas adsorption/desorption on the channel surface, which typically impacts V_{th} in oxide TFTs. In the present study, the use of a Y_2O_3 passivation layer over the IZO channel is believed to suppress gas interactions, thereby suppressing V_{th} shifts under NBS conditions.

Conversely, under PBS conditions, significant positive V_{th} shifts were observed in polycrystalline IZO TFTs with Zn concentrations of 9% (ΔV_{th} =0.74 V) and 86% (ΔV_{th} =0.8 V). The V_{th} shifts in this case are primarily attributed to electron trapping at the channel/insulator interface. Polycrystalline IZO channels are known to exhibit a higher density of interface states compared to their amorphous counterparts, largely due to increased surface roughness. For instance, the RMS indicates surface roughness of

polycrystalline IGZO annealed at 600 °C exceeds 4 nm, whereas amorphous IGZO exhibits a roughness of less than 0.4 nm.[29] This increased roughness has been linked to characteristic degradation in polycrystalline IGZO TFTs, such as reduced mobility and increased subthreshold swing.[30]

In the present study, the RMS was measured by AFM were 0.36 nm for amorphous IZO (25% Zn) and 0.80 nm and 0.90 nm for polycrystalline IZO with Zn concentrations of 9% and 86%, respectively (**Figure 4 - 3**). These results strongly suggest that the PBS-induced degradation is dominated by electron trapping at the polycrystalline/insulator interface.

Overall, the findings indicate that incorporating Zn into In_2O_3 not only enhances field-effect mobility but also improves the reliability of IZO TFTs under bias stress conditions.

4.4 Conclusion

I investigated the electron transport properties of IZO films and IZO TFTs across a range of *Zn a.t.%* (0%, 9%, 25%, 41%, 68%, and 86%). IZO films with *Zn a.t.%* between 25% and 68% retained an amorphous phase even after annealing at 300 ºC in air, whereas films with 9% and 86% Zn exhibited crystallization under the same conditions.

The carrier effective mass for all IZO films was determined to be between 0.1 m_0 and 0.2 m_0 independent of *Zn a.t.%.* This suggests that both In 5s and Zn 4s orbitals contribute

to electron transport in the studied Zn concentration range, but the overall band structure and density of states are not significantly affected by variations in Zn content.

Amorphous IZO TFTs with 25% Zn demonstrated superior performance, achieving the highest field-effect mobility μ_{FE} of 41 $cm^2 V^{-1} s^{-1}$, a subthreshold swing of 0.10 V dec^{-1}, and excellent reliability. In contrast, polycrystalline IZO TFTs exhibited significantly lower μ_{FE} values <12 $cm^2 V^{-1} s^{-1}$ due to the presence of grain boundaries. Additionally, these polycrystalline TFTs suffered from poor reliability under PBS, primarily caused by electron trapping at the polycrystalline/insulator interface. This phenomenon is linked to a higher density of interface states and structural defects at the interfaces.

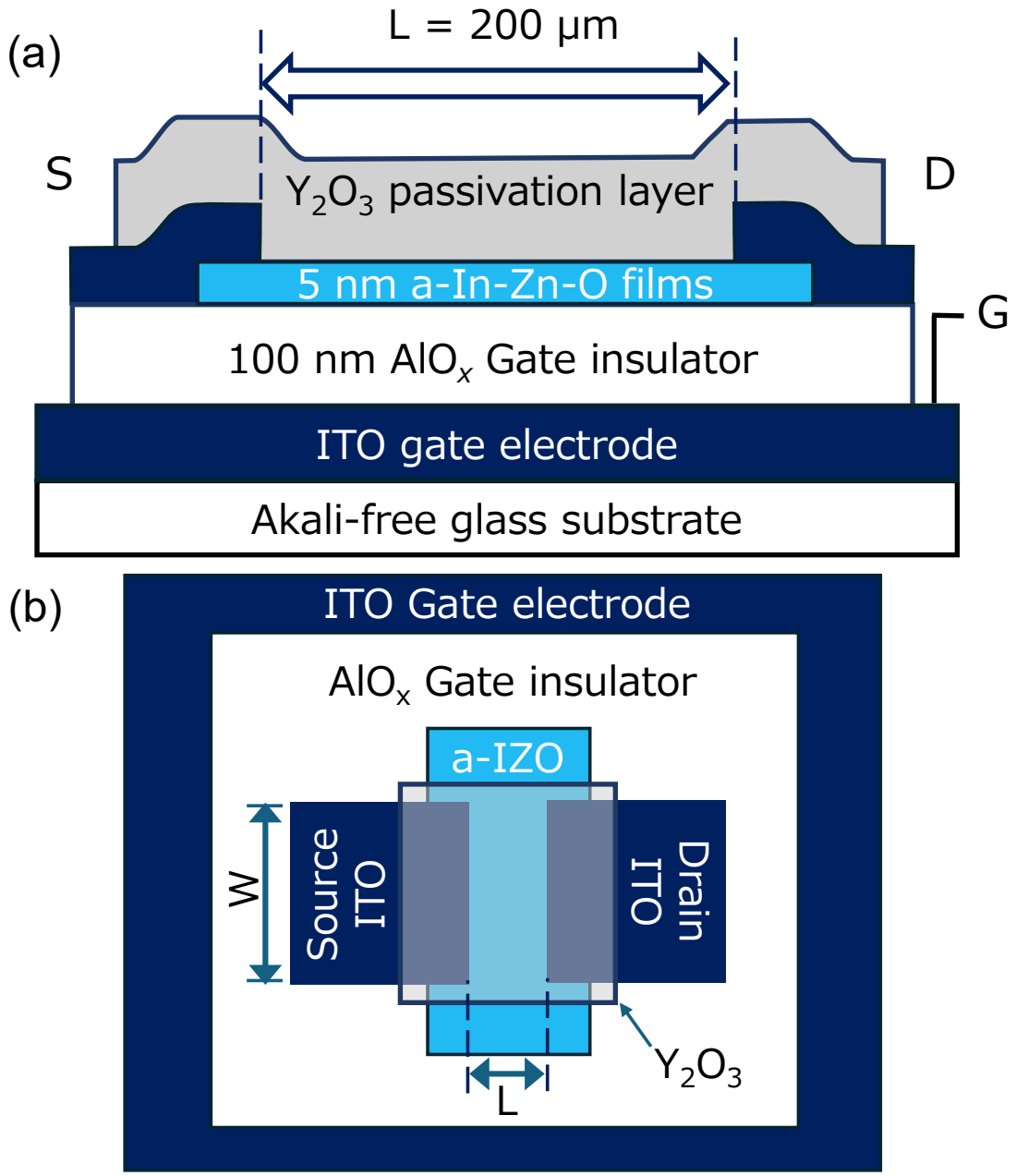

Figure 4 - 1 Schematic structure of bottom-gate & top-contact type IZO TFT

(a) section structure (b) top view

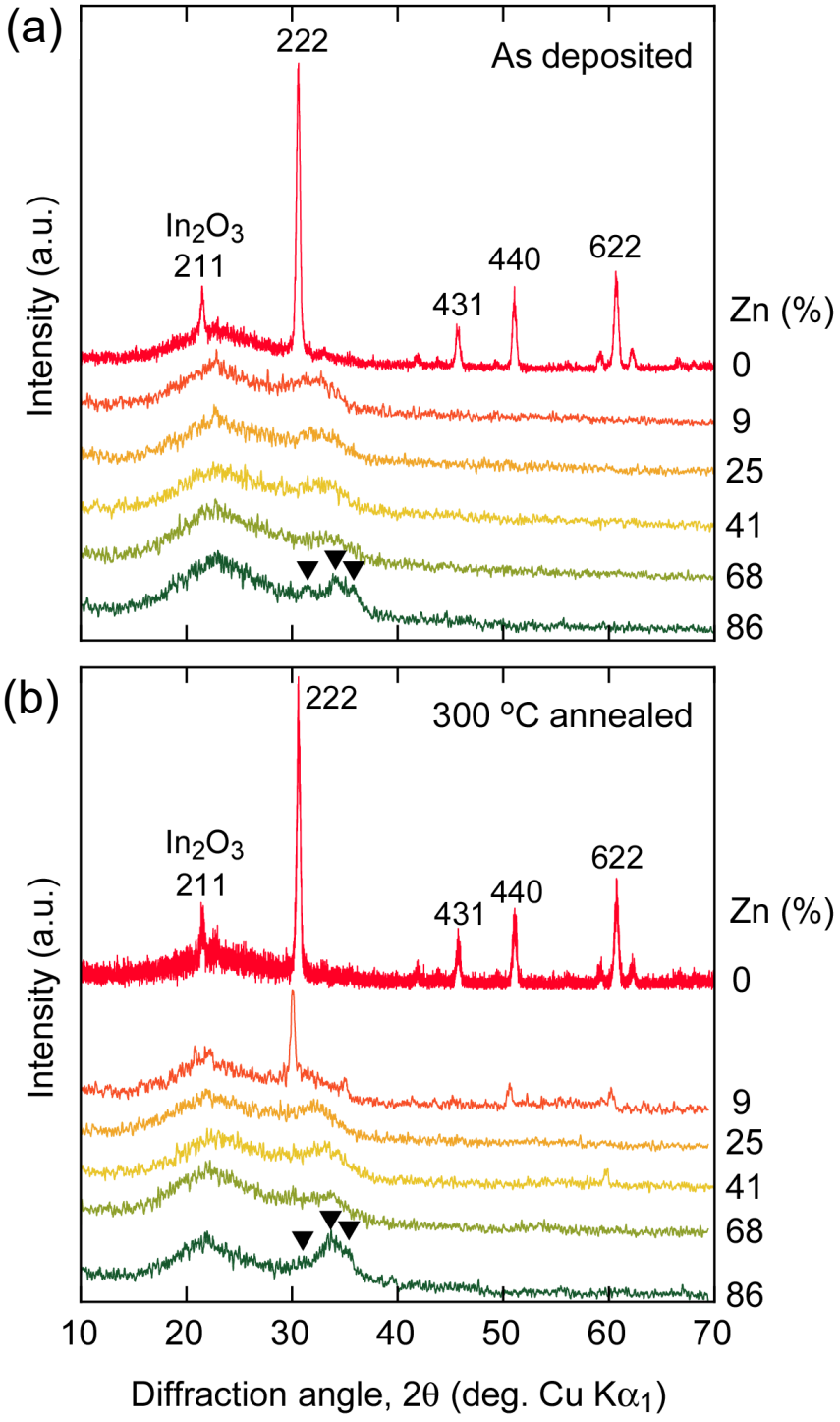

Figure 4 - 2 GIXRD pattern of resultant IZO films

(a) as deposited (b) annealed at 300oC

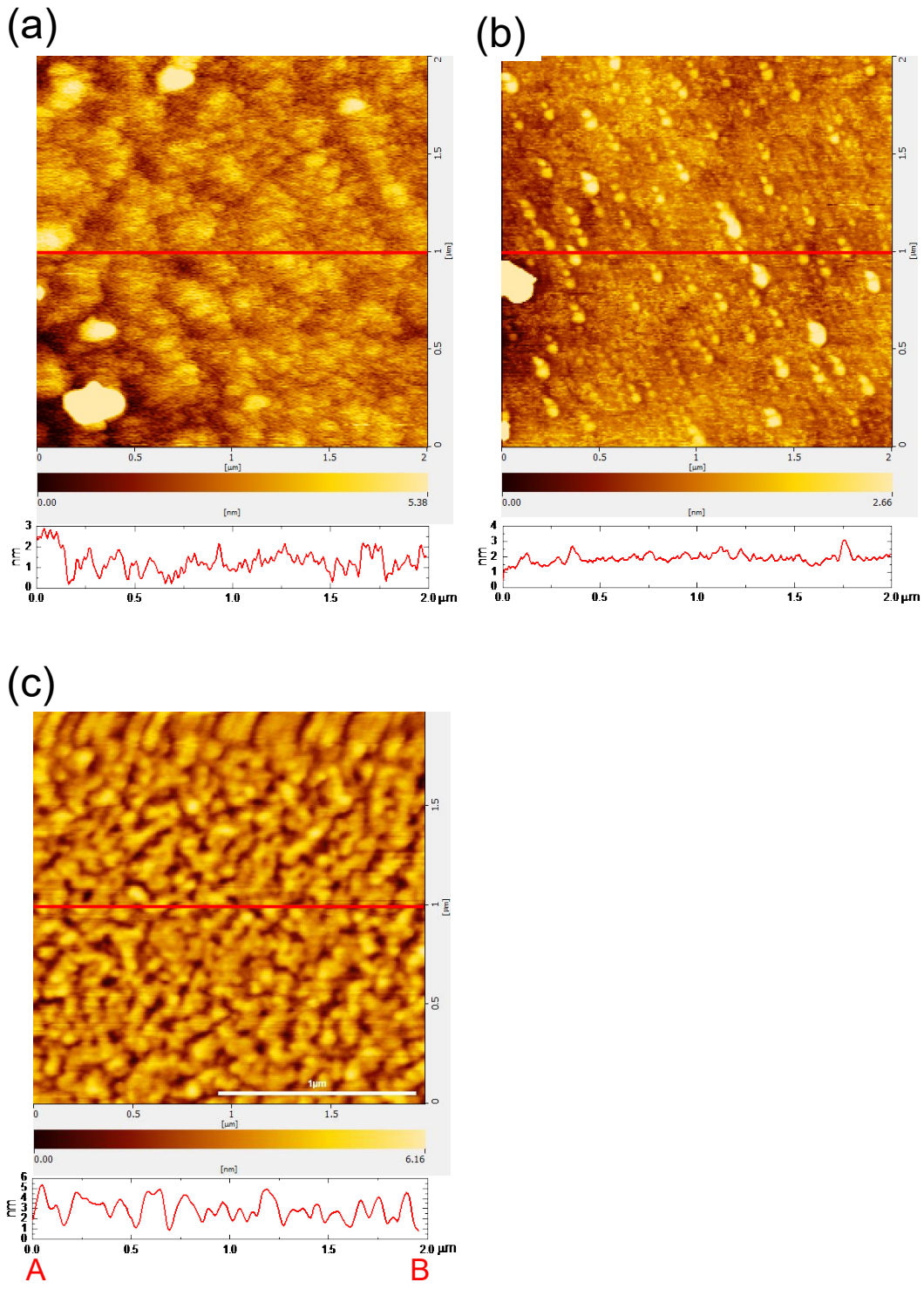

Figure 4 - 3 AFM images of IZO films with various *Zn a.t.%*

(a) *Zn a.t.%* = 9 % (b) *Zn a.t.%* = 25 % (c) *Zn a.t.%* = 86 %

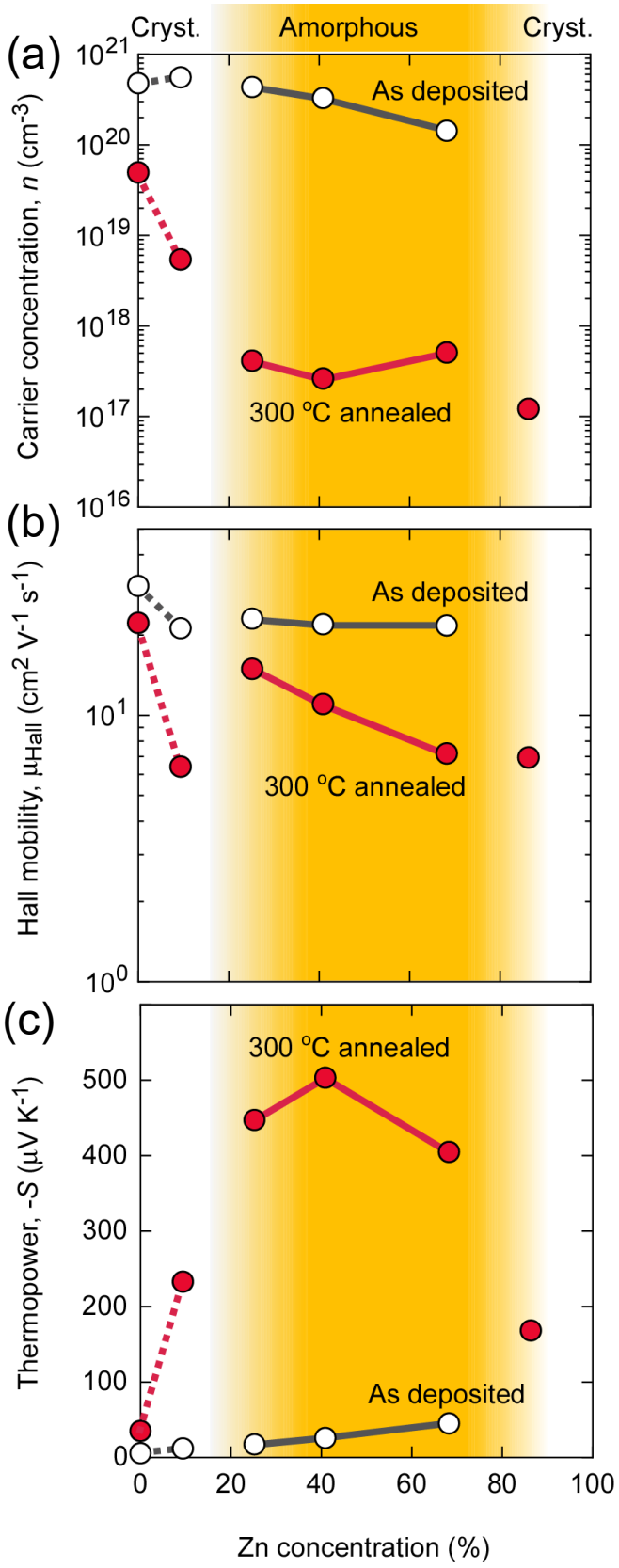

Figure 4 - 4 Electron transport properties of the IZO films at room temperature

(a) Carrier concentration

(b) Hall mobility

(c) Seebeck coefficient

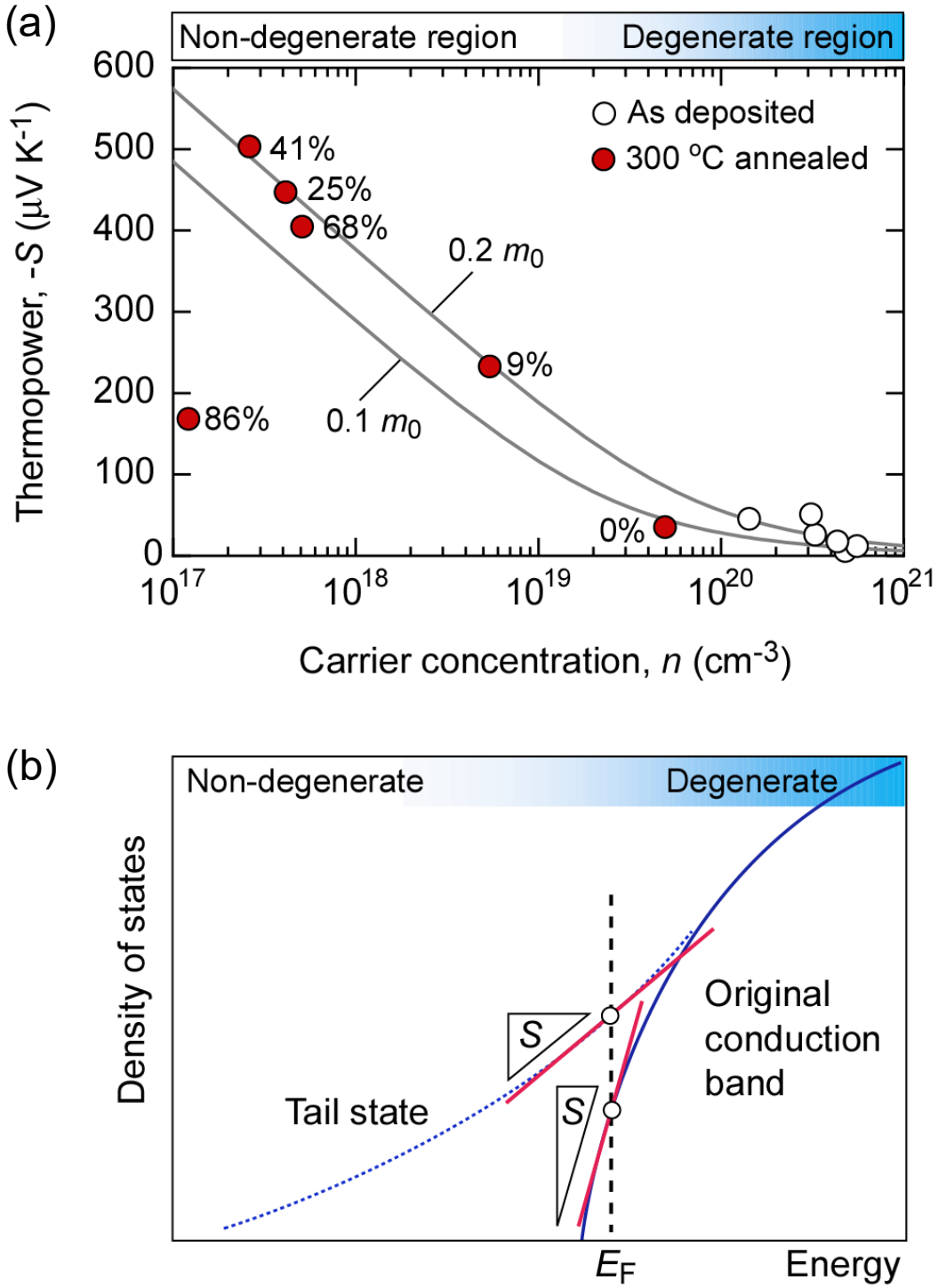

Figure 4 - 5 Thermopower of the IZO films with various Zn concentrations

(a) *S*–log *n* plot (b) Schematic *E*-dependence of the *DOS* around the *CBM* of 86 *Zn a.t.%*

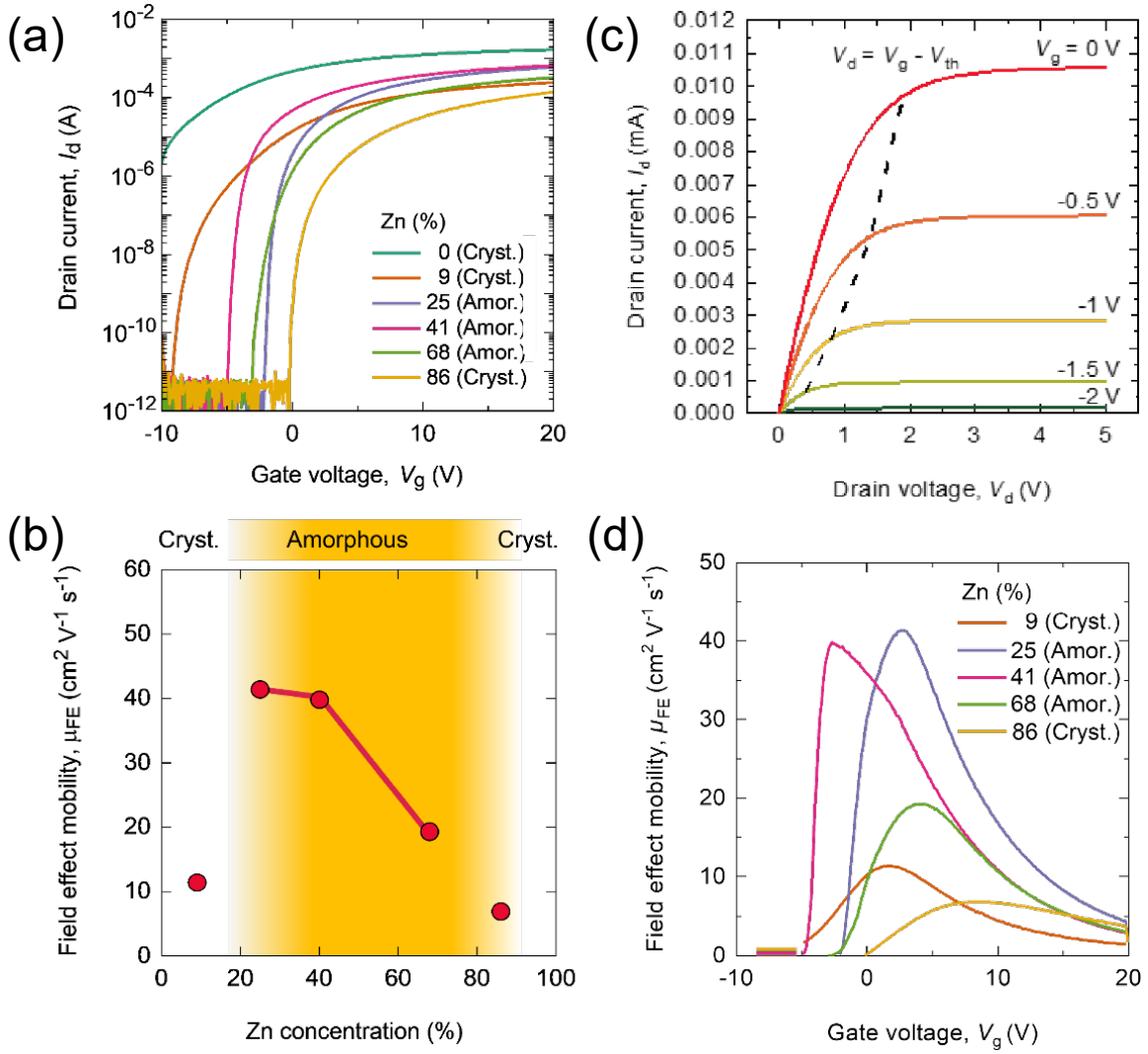

Figure 4 - 6 Typical transistor characteristics of the IZO TFTs at room temperature

(a) Transfer characteristics (b) Field-effect mobility (μ_{FE}) of the IZO TFTs

(c) Output characteristics of the IZO TFTs with 25% Zn (d) Relationship between μ_{FE} and V_g in IZO TFTs with various Zn concentrations

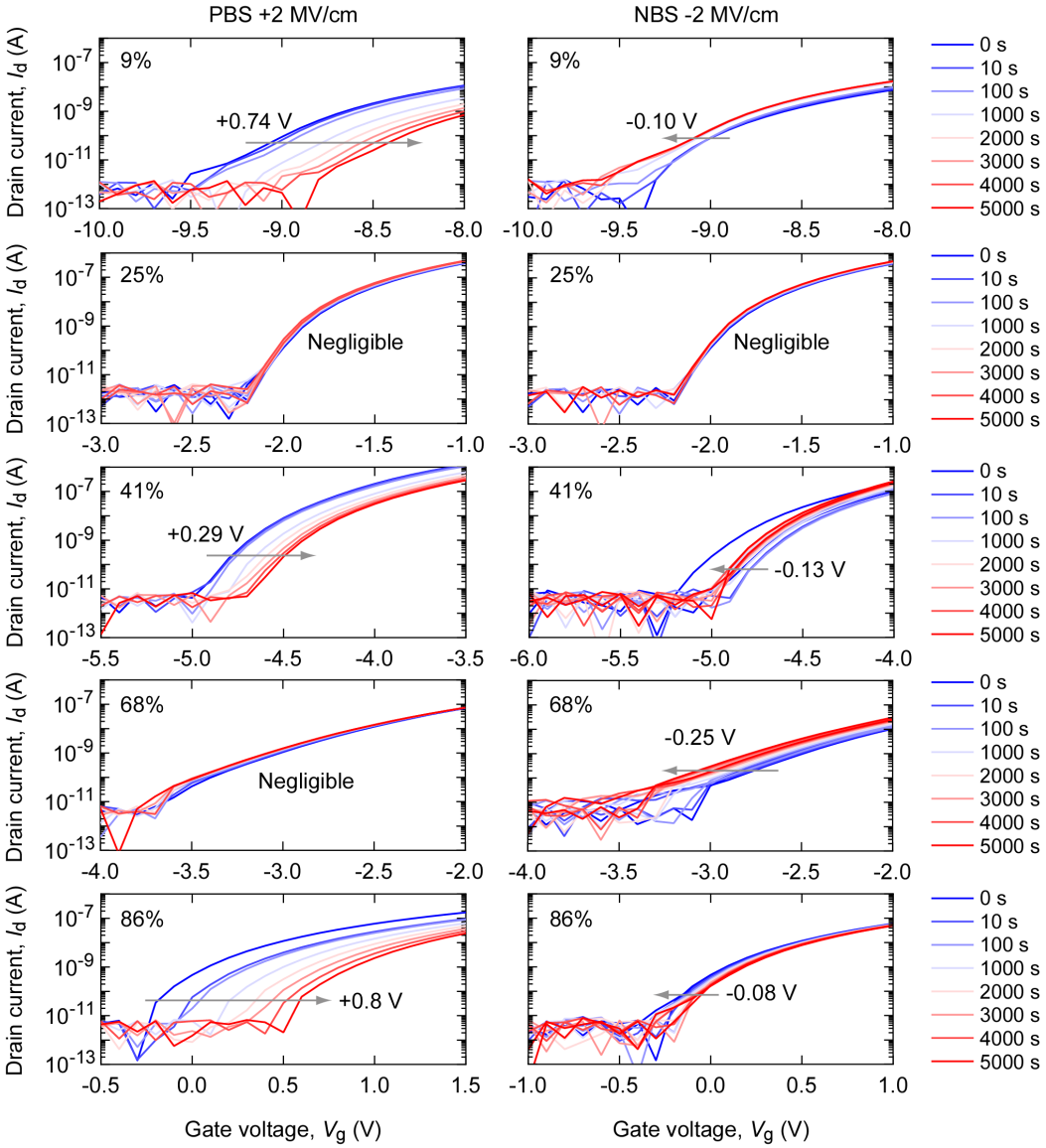

Figure 4 - 7 Change in the transfer characteristics of the IZO TFTs under PBS (+2 MV cm^{-1}) and NBS (−2 MV cm^{-1})

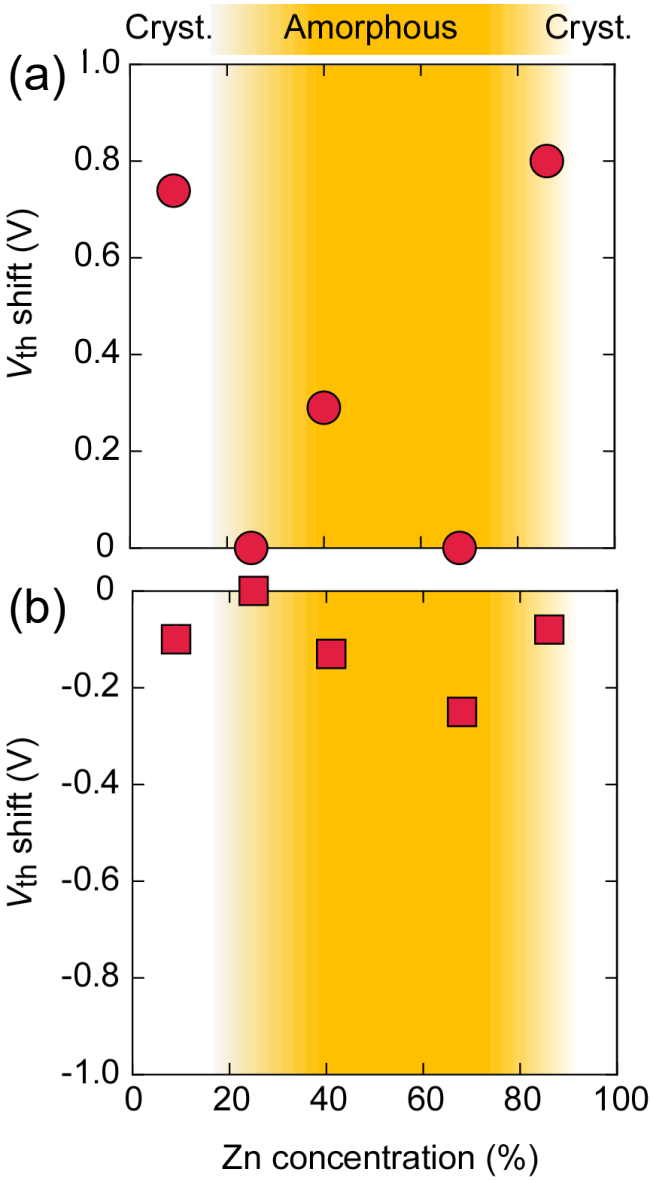

Figure 4 - 8 Stability of the IZO TFTs with different Zn concentrations

(a) PBS for 5000 s

(b) NBS for 5000 s

Table 1 Threshold voltage and subthreshold swing of the IZO TFTs with varied *Zn a.t.%*.

Zn a.t.% (%)	V_{th}(V)	*S.S.* (V/decade)
0	–11.0	N.D.
9	–8.6	0.25
25	–1.9	0.10
41	–4.7	0.13
68	–3.0	0.26
86	+0.3	0.11

Table 2 Bias voltage of PBS and NBS applying on channel layer with varied *Zn a.t.%*.

Zn a.t.% (%)	V_{GS}– V_{TH} (PBS) (V)	V_{GS} –V_{TH} (NBS) (V)
9	28.6	–11.4
25	21.9	–18.1
41	24.7	–15.3
68	23.0	–17.0
86	19.7	–20.3

Reference

[1] Kwon, J. Y. & Jeong, J. K. Recent progress in high performance and reliable n-type transition metal oxide-based thin film transistors. *Semicond. Sci. Technol.* **30**, 024002 (2015).

[2] Hara, Y., Kikuchi, T. *et al.* IGZO-TFT technology for large-screen 8K display. *J. Soc. Inf. Display* **26**, 169-177 (2018).

[3] Hendy, I., Brewer, J. *et al.* Development of high-performance IGZO backplanes for displays. *Information Display* **38**, 60-68 (2022).

[4] Kim, T., Choi, C. H. *et al.* Progress, Challenges, and Opportunities in Oxide Semiconductor Devices: A Key Building Block for Applications Ranging from Display Backplanes to 3D Integrated Semiconductor Chips. *Adv Mater* **35**, e2204663 (2023).

[5] Magari, Y., Kataoka, T. *et al.* High-mobility hydrogenated polycrystalline In2O3 (In2O3: H) thin-film transistors. *Nature communications* **13**, 1078 (2022).

[6] Jeong, J. K., Yang, H. W. *et al.* Origin of threshold voltage instability in indium-gallium-zinc oxide thin film transistors. *Appl. Phys. Lett.* **93**, 123508 (2008).

[7] Park, J. C., Lee, H. N. *et al.* Self-aligned top-gate amorphous indium zinc oxide thin-film transistors exceeding low-temperature poly-Si transistor performance. *ACS Appl Mater Interfaces* **5**, 6990-6995 (2013).

[8] Ji, H., Hwang, A. Y. *et al.* Improvement in Field-Effect Mobility of Indium Zinc Oxide Transistor by Titanium Metal Reaction Method. *Ieee T Electron Dev* **62**, 1195-1199 (2015).

[9] Yang, Z., Yang, J. W. *et al.* Influence of channel layer thickness on the stability of amorphous indium zinc oxide thin film transistors. *Mater Lett* **166**, 46-50 (2016).

[10] Zhao, J. W., Zhang, X. A. *et al.* Performances of transparent indium zinc oxide thin film transistors using ZrO

as dielectric processed by solution method. *Phys Status Solidi A* **214** (2017).

[11] Illiberi, A., Katsouras, I. *et al.* Atmospheric plasma-enhanced spatial-ALD of InZnO for high mobility thin film transistors. *J Vac Sci Technol A* **36** (2018).

[12] Lee, J. M., Lee, H. J. *et al.* All-oxide thin-film transistors with channels of mixed InOx-ZnOy formed by plasma-enhanced atomic layer deposition process. *J Vac Sci Technol A* **37** (2019).

[13] Sheng, J., Hong, T. *et al.* Design of InZnSnO Semiconductor Alloys Synthesized by Supercycle Atomic Layer Deposition and Their Rollable Applications. *Acs Appl Mater Inter* **11**, 12683-12692 (2019).

[14] Liu, M. Y., Kim, H. *et al.* Carrier Density-Tunable Work Function Buffer at the Channel/Metallization Interface for Amorphous Oxide Thin-Film Transistors. *Acs Appl*

Electron Ma **3**, 2703-2711 (2021).

[15] Cho, M. H., Choi, C. H. *et al.* Comparative Study of Atomic Layer Deposited Indium-Based Oxide Transistors with a Fermi Energy Level-Engineered Heterojunction Structure Channel through a Cation Combinatorial Approach. *Acs Appl Mater Inter* **14**, 18646-18661 (2022).

[16] Liang, Y.-K., Lin, J.-W. *et al.* Electrical characteristics of ultrathin InZnO thin-film transistors prepared by atomic layer deposition. *Ieee T Electron Dev* **70**, 1067-1072 (2023).

[17] Leenheer, A. J., Perkins, J. D. *et al.* General mobility and carrier concentration relationship in transparent amorphous indium zinc oxide films. *Physical Review B* **77**, 115215 (2008).

[18] Chang, S.-C. & Shiao, M.-H. Smooth indium zinc oxide film prepared by sputtering a In2O3: ZnO= 95: 5 target. *Microelectronics journal* **38**, 1202-1206 (2007).

[19] Jia, J., Nakamura, S. i. *et al.* Crystallization behavior during transparent In2O3-ZnO film growth. *physica status solidi (a)* **213**, 2291-2295 (2016).

[20] Feng, B., Lugg, N. R. *et al.* Direct Observation of Oxygen Vacancy Distribution across Yttria-Stabilized Zirconia Grain Boundaries. *ACS Nano* **11**, 11376-11382 (2017).

[21] Frischbier, M. V., Wardenga, H. F. *et al.* Influence of dopant species and concentration

on grain boundary scattering in degenerately doped In2O3 thin films. *Thin Solid Films* **614**, 62-68 (2016).

[22] Vining, C. B. A Model for the High-Temperature Transport-Properties of Heavily Doped N-Type Silicon-Germanium Alloys. *J Appl Phys* **69**, 331-341 (1991).

[23] Yang, H., Zhang, Y. Q. *et al.* Thermopower Modulation Analyses of High-Mobility Transparent Amorphous Oxide Semiconductor Thin-Film Transistors. *Acs Appl Electron Ma* **4**, 5081-5086 (2022).

[24] Ghediya, P., Yang, H. *et al.* Improved Electron Transport Properties of Zn-Rich In-Ga-Zn-O Thin-Film Transistors. *J Phys Chem C* (2023).

[25] Ohta, H., Huang, R. *et al.* Large enhancement of the thermoelectric Seebeck coefficient for amorphous oxide semiconductor superlattices with extremely thin conductive layers. *physica status solidi (RRL)–Rapid Research Letters* **2**, 105-107 (2008).

[26] Jia, J. J., Oka, N. *et al.* Direct observation of the band gap shrinkage in amorphous InO-ZnO thin films. *J Appl Phys* **113** (2013).

[27] Orita, M., Ohta, H. *et al.* Amorphous transparent conductive oxide InGaO3 (ZnO) m (m≤ 4): a Zn4s conductor. *Philosophical magazine B* **81**, 501-515 (2001).

[28] Abe, K., Sato, A. *et al.* Mobility-and temperature-dependent device model for amorphous In–Ga–Zn–O thin-film transistors. *Thin Solid Films* **559**, 40-43 (2014).

[29] Nomura, K., Takagi, A. *et al.* Amorphous oxide semiconductors for high-performance flexible thin-film transistors. *Japanese journal of applied physics* **45**, 4303 (2006).

[30] Hanyu, Y., Abe, K. *et al.* Effects of high-temperature annealing on operation characteristics of a-In-Ga-Zn-O TFTs. *Journal of Display Technology* **10**, 979-983 (2014).

Chapter 5 Effective thickness of Zn-incorporated In_2O_3 Thin-Film Transistor

5.1 Object of this chapter

Among the numerous reports on TOS- TFTs, polycrystalline indium oxide In_2O_3-based TFTs with large grain sizes (~several micrometers) have been identified as promising candidates due to their high field-effect mobility μ_{FE} of approximately 100 $cm^2\ V^{-1}\ s^{-1}$.[1,2] However, a significant drawback of these devices is their poor reliability, primarily attributed to gas absorption at the channel surface and grain boundaries.[2] To address this issue, two main strategies have been proposed. The first involves the application of passivation layers; for instance, the effectiveness of Y_2O_3 passivation in improving device reliability.[3] The second strategy focuses on stabilizing the amorphous phase of In_2O_3 by incorporating an appropriate concentration of Zn as what was described in Chapter 4.

While homologous crystalline phases of $In_2O_3(ZnO)_m$ ($m \geq 3$, integer) exist within the IZO system, their high crystallization temperature (>500 °C) favors the stabilization of the amorphous phase under typical fabrication conditions[4-8]. The research in Chapter 4 has shown that an amorphous phase is maintained when the Zn concentration in IZO films falls within the range of 25% to 68% after 300ºC annealing. Amorphous IZO-TFTs in

this range not only stabilize the structure but also exhibit higher μ_{FE} values (~40 $cm^2\ V^{-1}\ s^{-1}$) compared to their polycrystalline counterparts.

In this chapter, I mainly discuss the origin of the μ_{FE} differences between amorphous and polycrystalline IZO channels. I performed electric field thermopower modulation analysis on both amorphous and polycrystalline IZO-TFTs to measure variations in effective thickness as a function of V_{GS}. For the amorphous IZO channel, the effective thickness was observed to be zero when $V_{GS} - V_{TH}$ equal to zero, gradually increasing with $V_{GS} - V_{TH}$ to a maximum of approximately 1.6 nm, consistent with conduction band bending. By contrast, the polycrystalline IZO channel exhibited an initial effective thickness of approximately 5 nm in the absence of gate voltage, which rapidly decreased to around 1.7 nm upon gate bias application.

These findings suggest that electron transport in amorphous IZO channels is governed by field-effect theory, with carrier mobility enhanced by the uniformity of the amorphous structure. On the contrast, in polycrystalline IZO channels, electron transport is dominated by grain boundaries, which introduce localized defects and trap states, thereby limiting mobility.

5.2 Experiment

Fabrication of IZO-TFTs.

The IZO-TFTs (bottom-gate and top-contact type) were fabricated on ITO-coated alkaline-free glass substrates. A 100-nm-thick amorphous a-Al_2O_3 gate insulator was deposited on the substrate by ALD technique, the dielectric permittivity (ε_r) and capacitance (C_i) of the a-Al_2O_3 films were 8 and 70 nF cm^{-2} respectively. Subsequently, 5-nm-thick IZO films were deposited using PLD from ceramic IZO target with various *Zn a.t.%* at room temperature in 3 Pa oxygen. The laser fluence was maintained at approximately 1.5 J cm^{-2} $pulse^{-1}$. The composition of resultant IZO films was measured using ICP-MS. The IZO films were then annealed in ambient air at 300 °C for 1 h. After annealing, ITO source/drain electrodes were deposited using PLD. In order to suppress the degeneration from atmosphere, a thick Y_2O_3 film of approximately 50 nm was deposited by PLD as passivation layer. The devices were annealed at 300 °C in ambient air for 0.5 h. Notably, the IZO, ITO, and Y_2O_3 films were deposited using a stencil mask, where the *L* and width *W* were regulated in 200 μm and 400 μm respectively. The details of the TFT fabrication are described in Chapter 4.

Electric Field Thermopower Modulation Analyses.

The transfer characteristics of the IZO TFTs were evaluated using a semiconductor

device analyzer (B1500A, Agilent Technologies) at room temperature under dark conditions. Electric field thermopower modulation analyses were performed in air at room temperature. In detail, the thermopower modulation measurements were performed with 2 two Peltier devices placed beneath the IZO TFT. The temperature difference was monitored with two K-type thermocouples (150 μm in diameter, SHINNETSU Co.) mechanically attached to the channel edges. Chapter 2 detailed described the thermopower modulation analyses.

5.3 Result and discussion

The effective channel thickness of the IZO TFTs was investigated across a range of *Zn a.t.%* = 9%, 25%, 41%, 68%, and 86%. As discussed in Chapter 3, the *Zn a.t.%* = 9% and 86% resulted in polycrystalline structures, whereas intermediate concentrations of 25%, 41%, and 68% were stabilized as amorphous structures. Compared to their polycrystalline which exhibited μ_{FE} of ~ 10 cm^2V^{-1}, the amorphous IZO TFTs exhibited significantly higher field-effect mobility μ_{FE} values of approximately 41 $cm^2\ V^{-1}\ s^{-1}$. These results indicate the superior charge transport properties of amorphous IZO films. **Figure 5 - 1** and **Table 3** shows he data of the IZO film properties and transistor characteristics

Figure 5 - 2 describe the schematic relationship between ΔT and ΔV of a TFT based

on n-type semiconductor like In-Zn-O channel. For an n-type channel, the Seebeck coefficient *S* generally exhibits a dependency on the gate voltage: at low V_{GS} values, *S* is larger compared to high V_{GS} values. This trend is attributed to the stronger electric field in channel induced higher carrier concentrations, which negatively correlated to Seebeck coefficient.

Figure 5 - 2 a illustrates the typical $\Delta T-\Delta V$ plots for the IZO TFT with a Zn concentration of 25% under varying V_{GS} at room temperature. The *S* values are negative, confirming that the channel exhibits n-type semiconductor behavior. For instance, when $V_{GS}-V_{TH}=+10$ V, the measured *S* is -80 $\mu V K^{-1}$, while at $V_{GS}-V_{TH}=+20$ V, *S* decreases to -56 μV K^{-1}. This reduction reflects an increase in the volumetric carrier concentration n_{3D} within the channel with increasing gate voltage, consistent with the standard field-effect principle.

Figure 5 - 2 b presents the dependence of *S* on the sheet carrier concentration n_{2D}, which is calculated with the equation that $n_{2D}=C_i(V_{GS}-V_{TH})$ as described in Chapter 2. A notable difference exhibited in the behavior of *S* with respect to n_{2D} between amorphous and polycrystalline channels. The slope of the *S* vs. log n_{2D} plot is lower for the amorphous IZO TFTs (*Zn a.t.%* = 25%, 41%, and 68%) compared to the higher slope observed for polycrystalline IZO TFTs (*Zn a.t.%* = 9% and 86%).

For comparison, the Seebeck coefficient *S* values of the IZO films were independently measured as discussed in Chapter 4. The DOS effective mass m^* was calculated for IZO films with *Zn a.t.%* other than 86%, revealing that m^* ranged from 0.1 m_0 - 0.2 m_0. For the *Zn a.t.%* of 86%, the presence of unlined value due to tail states near the conduction-band minimum contributed to the observed reduction in *S*.

Figure 5 - 4 illustrates the effective channel thickness t_{eff} of the IZO TFTs, derived from n_{2D}/n_{3D}. Based on the comparison between the -*S* vs. log n_{2D} plot and the -*S* vs. log n_{3D} plot, as a function of $V_{gseff} = \underline{V_{GS}} - V_{TH}$. For the amorphous channels (*Zn a.t.%* = 25%, 41%, and 68%), t_{eff} was initially zero at V_{gseff} = 0 V, and it progressively increased with increasing $\underline{V_{GS}} - V_{TH}$. This indicates that the t_{eff} in the amorphous TFTs is dynamically modulated by the applied gate voltage, consistent with field-induced accumulation behavior.

In contrast, the polycrystalline channels (*Zn a.t.%* = 9% and 86%) exhibited relatively large t_{eff} values even at small V_{gseff}. As V_{gseff} increased, t_{eff} gradually approached a saturation value of approximately 1.7 nm, comparable to the saturation effective thickness observed for amorphous channels. This difference in behavior between amorphous and polycrystalline channels suggests that the gate voltage plays a primary role in controlling the effective channel thickness of amorphous IZO TFTs, the polycrystalline channels are

influenced by additional factors, such as structural inhomogeneities and the presence of grain boundaries.

Figure 5 - 5 provides a detailed comparison of the electronic transport mechanisms in IZO TFTs with amorphous and polycrystalline channels based on the t_{eff} results. For the amorphous channel, the E_F is positioned below the CBM in the absence of an applied gate electric field, as depicted in **Figure 5 - 5 a**. When a positive gate voltage is applied, band bending occurs at the a-Al_2O_3/IZO heterointerface which are in the function of gate insulator and channel respectively. This leads to the formation of a two-dimensional electron gas at the interface, facilitating carrier accumulation, as illustrated in **Figure 5 - 5 b**. The behavior of the amorphous channel is consistent with the standard field-effect theory for nondegenerate semiconductors, where the accumulation layer is directly controlled by the gate electric field[9]. Such a mechanism demonstrates the importance of gate modulation in achieving high-performance characteristics in amorphous IZO TFTs.

On the contrast, the polycrystalline channel exhibits markedly different behavior. A spontaneously formed conducting layer, which thickness approximately equal to 5 nm which close to the total film thickness of the IZO layer, exists even in the absence of a gate electric field, as shown in **Figure 5 - 5 c**. This phenomenon appears because the E_F of polycrystalline IZO lies above the CBM, resulting in a degenerate conduction channel.

However, electron mobility in the polycrystalline channel is restricted by the presence of grain boundaries, which introduces a double Schottky barrier along the channel. When E_F is relatively low, even at a gate voltage of V_{GS} = +20 V, the potential barriers suppress carrier transport significantly as illustrated in **Figure 5 - 5 d.**

These findings suggested that there was a difference in transport mechanisms between amorphous and polycrystalline IZO channels. Electron transport in the amorphous IZO channel is primarily dominated by V_{GS} induced carrier modulation as the standard field-effect framework. However, in the polycrystalline channel, structural factors such as grain boundaries and associated potential barrier effects dominate, limiting mobility and hindering the t_{eff} modulated with V_{GS}. These differences suggested the critical role of channel microstructure in determining the electrical properties and operational efficiency of IZO TFTs.

5.4 Conclusion

The electric field thermopower modulation analyses were conducted to investigate the changes in t_{eff} of amorphous and polycrystalline IZO TFTs as a function of V_{GS}. For the amorphous IZO channel, the t_{eff} was initially zero at V_{geff} = 0 V, indicating the absence of

significant carrier accumulation. As V_{geff} increased, the t_{eff} increased and reached a maximum of approximately 1.6 nm. This behavior suggests conduction band bending at the Al_2O_3/IZO heterointerface, consistent with the formation of a two-dimensional electron gas under the influence of the gate electric field. These observations align with the standard field-effect theory for nondegenerate semiconductors, where gate modulation plays a critical role in controlling carrier accumulation and transport.

On the contrast, the polycrystalline IZO channel exhibited an initial t_{eff} of approximately 5 nm roughly equal to the total film thickness of the IZO layer even in the absence of V_{GS}. This indicates the presence of a pre-existing conduction path, probably coming from the Fermi level E_F positioned above the CBM. As $V_{GS} - V_{TH}$ increased, the t_{eff} rapidly decreased and converged to approximately 1.7 nm, suggesting a more confined electron transport region. This behavior differs fundamentally from that of the amorphous channel and suggests the influence of structural factors unique to polycrystalline materials. The sharp decrease in effective thickness for the polycrystalline channel can be attributed to potential barriers at grain boundaries, such as double Schottky barriers, which limit electron mobility and disturbed uniform gate-induced modulation. These findings suggest the contrasting transport mechanisms in amorphous and polycrystalline IZO TFTs. While electron transport in the amorphous channel follows the principles of standard field-effect

theory, the polycrystalline channel is dominated by microstructural effects, emphasizing the need for careful material design and processing to optimize device performance.

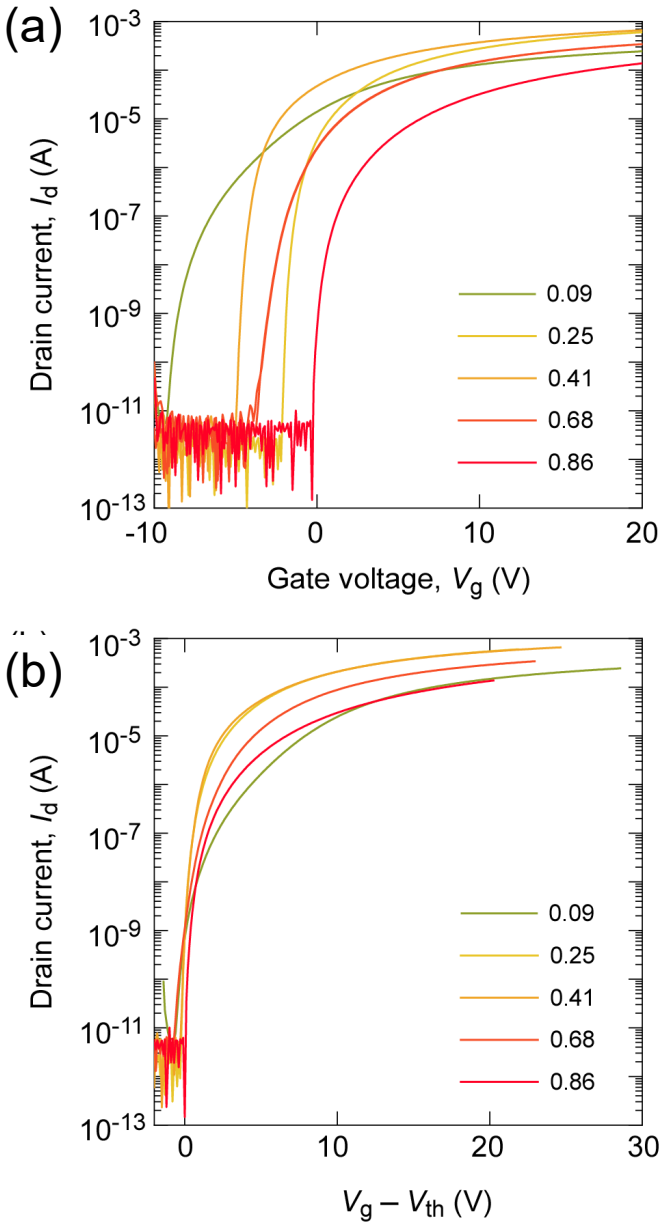

Figure 5 - 1 Typical transfer characteristics of the IZO TFTs at room temperature.

(a) Drain current modulated with gate voltage V_{GS}

(b) Drain current modulated with effective gate voltage V_{GSeff}

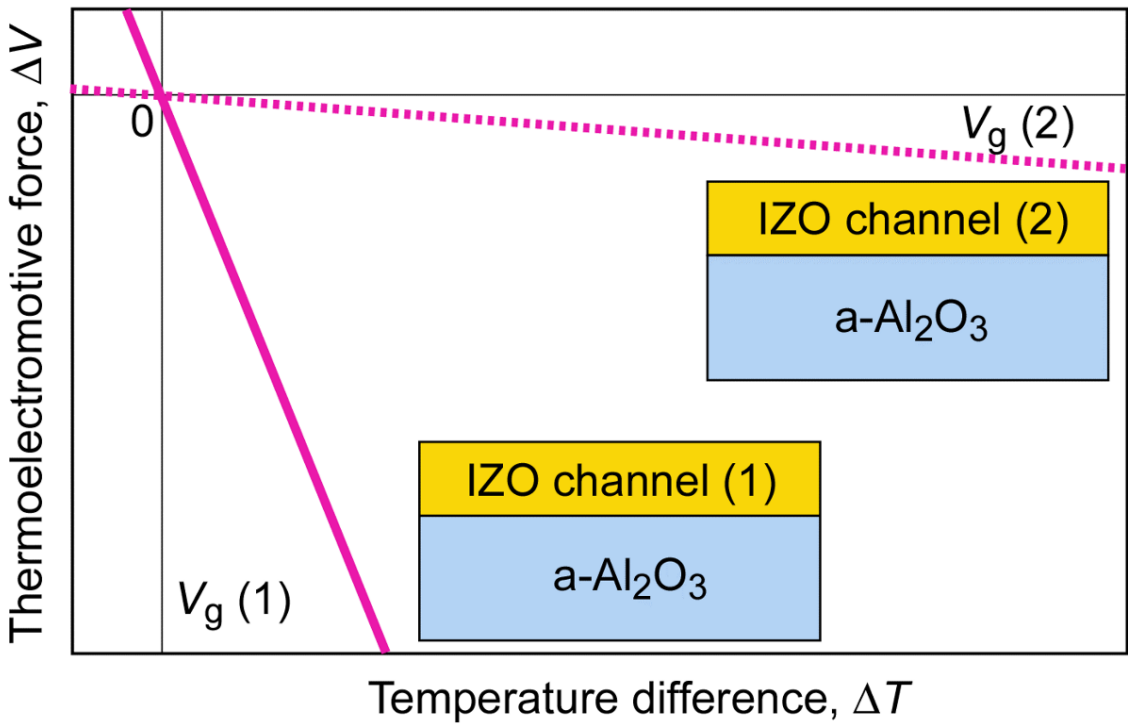

Figure 5 - 2 Schematic relationship between *ΔT* and *ΔV* of a TFT based on n-type semiconductor like In-Zn-O channel.

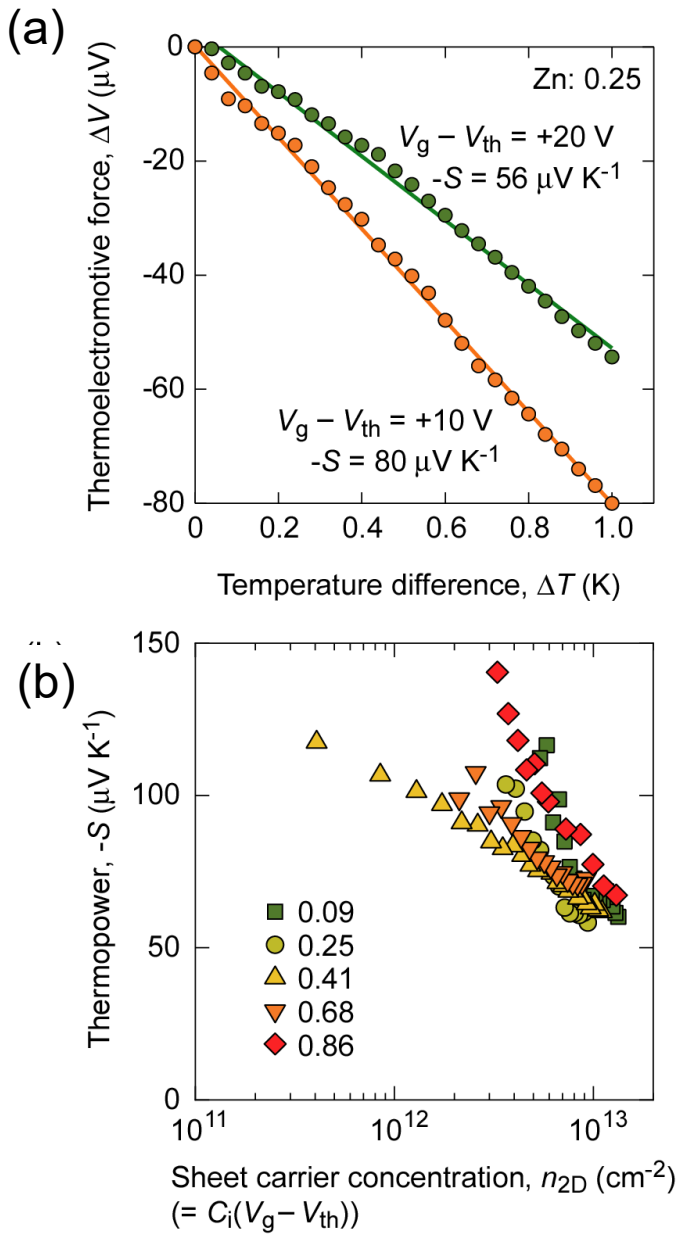

Figure 5 - 3 Thermopower of the IZO-TFTs

(a) ΔT–ΔV plots for the IZO (*Zn a.t. %* = 25 %) -TFT upon V_{GS} applications at room temperature. (b) Changes in S for the IZO-TFTs as a function of n_{2D}.

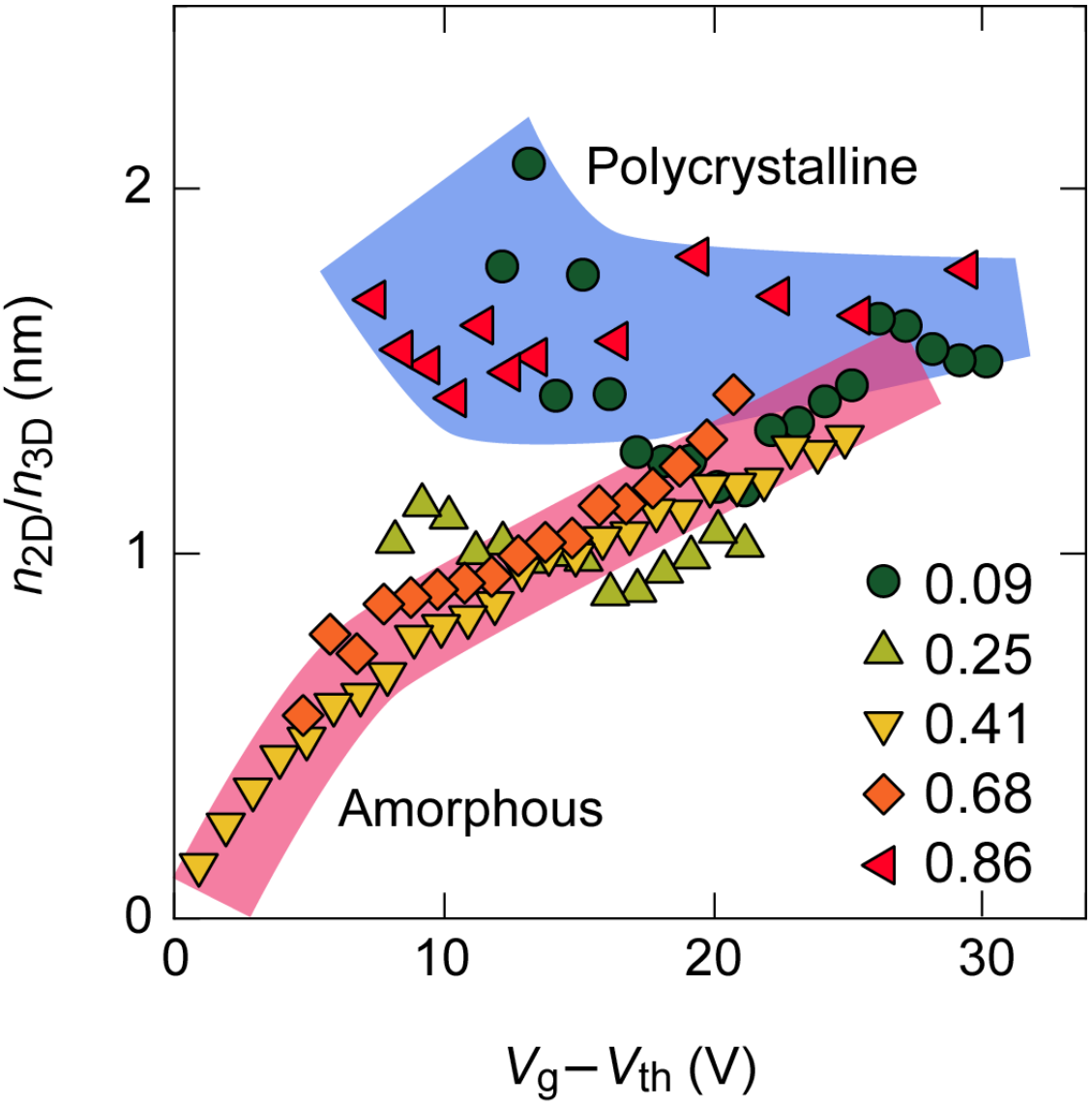

Figure 5 - 4 Effective channel thickness (n_{2D}/n_{3D}) of the IZO-TFTs as a function of

$V_{GSeff} = V_{GS} - V_{TH}$

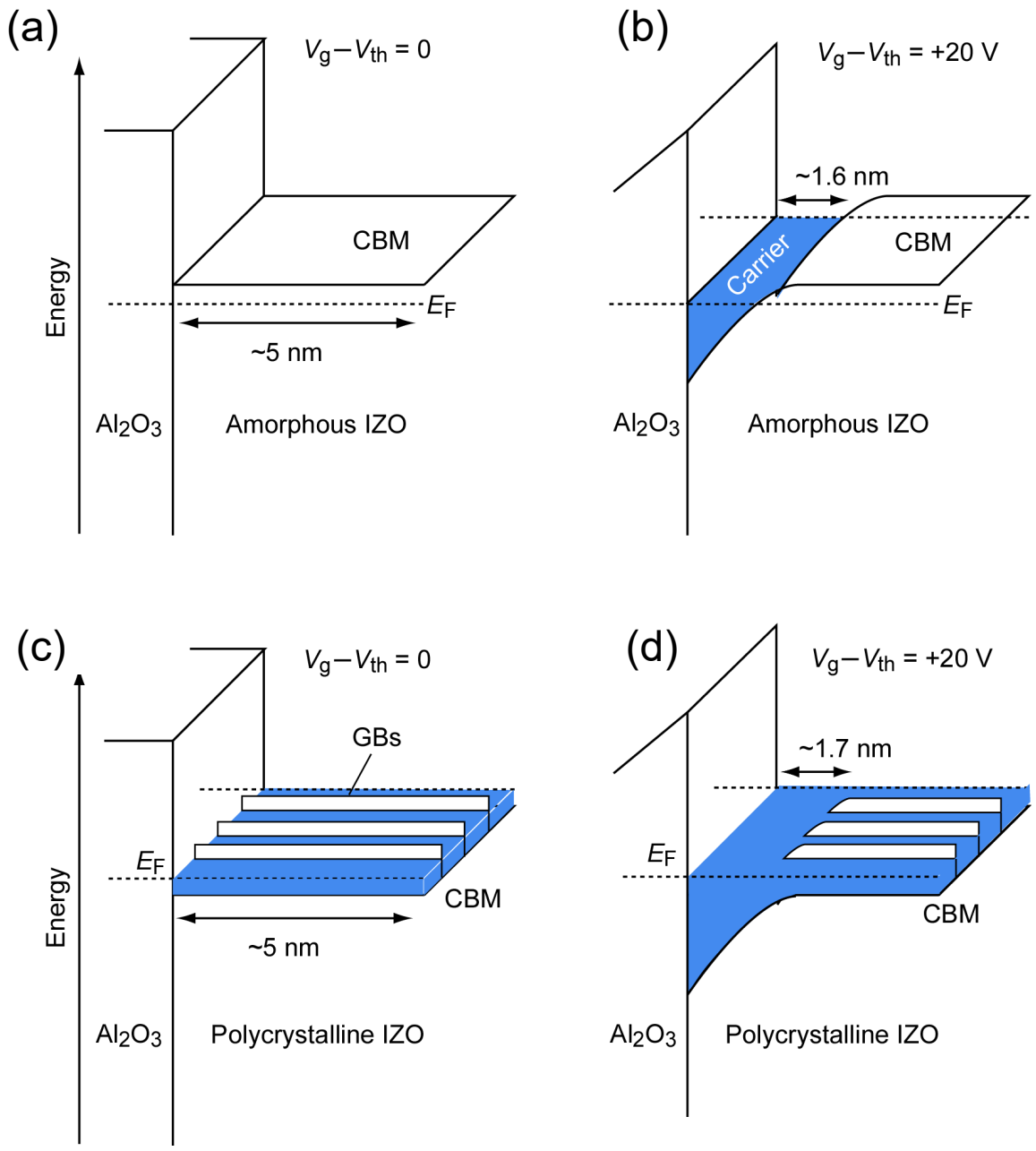

Figure 5 - 5 Schematic operation mechanism of the IZO-TFTs with amorphous channel and polycrystalline channel.

(a) amorphous channel with V_{GSeff} = 0 and (b) V_{GSeff} = 20 V

(c) polycrystalline channel with V_{GSeff} = 0 and (d) V_{GSeff} = 20 V

Table 3 Field-effect mobility, threshold voltage, and subthreshold swing of the IZO-TFTs with varied Zn concentration.

Zn a.t.%	μ_{FE} ($cm^2\ V^{-1}\ s^{-1}$)	V_{TH} (V)	*S.S.* (V/decade)
0.09	11.4	–8.6	0.25
0.25	41.4	–1.9	0.10
0.41	39.8	–4.7	0.13
0.68	19.3	–3.0	0.26
0.86	6.9	+0.3	0.11

Reference

[1] Jeong, J. K., Won Yang, H. *et al.* Origin of threshold voltage instability in indium-gallium-zinc oxide thin film transistors. *Applied Physics Letters* **93** (2008).

[2] Magari, Y., Kataoka, T. *et al.* High-mobility hydrogenated polycrystalline In2O3 (In2O3: H) thin-film transistors. *Nature communications* **13**, 1078 (2022).

[3] Ghediya, P. R., Magari, Y. *et al.* Reliable Operation in High-Mobility Indium Oxide Thin Film Transistors. *Small Methods*, 2400578 (2024).

[4] Barquinha, P., Goncalves, G. *et al.* Effect of annealing temperature on the properties of IZO films and IZO based transparent TFTs. *Thin Solid Films* **515**, 8450-8454 (2007).

[5] Lee, C., Lee, W. *et al.* Influence of annealing atmosphere on the structure, resistivity and transmittance of InZnO thin films. *Ceramics international* **34**, 1089-1092 (2008).

[6] Nomura, K., Ohta, H. *et al.* Room-temperature fabrication of transparent flexible thin-film transistors using amorphous oxide semiconductors. *nature* **432**, 488-492 (2004).

[7] Nomura, K., Takagi, A. *et al.* Amorphous oxide semiconductors for high-performance flexible thin-film transistors. *Japanese journal of applied physics* **45**, 4303 (2006).

[8] Yaglioglu, B., Yeom, H.-Y. *et al.* Crystallization of amorphous In2O3–10 wt% ZnO thin films annealed in air. *Applied Physics Letters* **86** (2005).

[9] Sze, S. M., Li, Y. *et al. Physics of semiconductor devices*. John wiley & sons, (2021).

Chapter 6. Summary

The given doctoral thesis focused on systematically investigating the effect of Zn incorporation into In_2O_3 on films and TFTs. For IZO films, Zn concentration effect on annealing effect, electron transport properties were mainly investigated. On the other hand, Zn concentration effect on the TFT performance and t_{eff} which are highly related with electric properties were highly discussed.

Firstly, the structural and electrical properties of IZO films with varying Zn concentration and annealing conditions were explored as a pre-experiment for follow-up research in chapter 4 and 5. GIXRD revealed that 100 nm IZO films with *10 wt.% Zn* crystallized after 300 ºC annealing, while other IZO films being amorphous structures. The Hall measurement revealed partial recovery of oxygen vacancies reduced carrier concentration at 200 ºC, whereas at 300 ºC, oxygen vacancy suppression decreases carrier concentration to ~ 10^{17} magnitude, which is lower than common reported carrier concentrations ~ 10^{20}.

In chapter 4, I detailed investigate the electrical transport properties of 300 ºC annealed IZO films and TFTs across a wide range of Zn concentrations (9–86 *Zn a.t. %*, observed with ICP-MS), which correspond different crystallized nature. In amorphous IZO films,

mobility decreases with increasing Zn content due to reduced carrier concentration. DOS effective mass remained $0.2m_0$ independent with Zn concentrations. Amorphous IZO TFTs with *25 a.t.%* Zn exhibited superior performance with a μ_{FE} of 41 cm^2/V s, a subthreshold swing of 0.10 V/decade, and excellent reliability. In contrast, polycrystalline TFTs showed μ_{FE} values below 12 cm^2/Vs as well as poor reliability under NBS and PBS treatment.

In chapter 5, electric field thermopower modulation analyses were proceeded to observed changes in effective thickness t_{eff} of amorphous and polycrystalline IZO TFTs as a function of effective gate voltage V_{GSeff}, and so that investigate the operating mechanism in different crystallinity. For amorphous IZO, teff increased with V_{geff}, and converse to 1.6 nm, followed well with field-effect theory. In polycrystalline IZO, t_{eff} started at 5 nm and decreased to 1.7 nm with increasing V_{geff}, due to fermi-level located above conduction band minimum when V_{geff}, is zero.

As summery, a systematically research on the muti-factors effect on the electric transport of IZO was investigated, including thickness, annealing temperature, crystallinity affect both properties of films and performance of devices. The conclusion demonstrates an optimal performance in proper Zn incorporation of IZO. The investigation of this research will provide a foundation on IZO TFT development, which

has a big chance to be utilized in next-generation display.

Acknowledgement

The given thesis and the included research were kindly conducted under the supervision of Prof. Hiromichi Ohta at Research Institute for Electronic Science, Hokkaido University from July 2022 (start from Proposal) to November 2024 (finished with 2 Paper accepted).

First of all, I would like to express my sincere gratitude to my supervisor, Prof. Hiromichi Ohta (RIES, Hokkaido U.), for his guidance and continuous support during my Master and PhD study. Especially, the supports contain lots of aspects: not only supports in research, knowledge as a supervisor, but also many supports on financial and official item such as scholarship application, RA, VISA application *etc.* I could never forget that at my first 2 years stay in Sapporo in 2017, his attentive guidance helped me quickly understand the different culture. During research, he always accurately and efficiently solves problems. These admirable traits will remain my unwavering pursuit and serve as the most value able asset in my future career.

Secondly, I would like to offer my special thanks to Prof. Yusaku Magari (RIES, Hokkaido U.). He is an expert on semiconductors. Discussing research topics with him always smooth even though I speak in poor but fast English with messy ideas. He is also

a gentle person and a very good listener, sharing with him the daily life was always comfortable.

I would also offer my special thanks to Prof. Hai Jun Cho (RIES, Hokkaido U. until 2022.8, currently at U. Ottawa). He brought me into the condensed matter physics field, especially heat conductance in nanometer scale. Besides his positive attitude to research and ideas in research, there is no doubt that he is a good teacher due to his solid foundation in theory and the simple explanation for complex concepts. As well, when I cannot convey my thoughts in English in my first several years in Sapporo, he always understood even though my logic is confusing. He always being nice to everyone and celebrated Birthday to every student and colleague.

I am deeply grateful to all lab members I have worked together with in Ohta lab. Dr. Anup Kumar Sanchela (OB, Professor at Pandit Deendayal Energy U.), Dr. Yuqiao Zhang (OB, Professor at Jiangsu U.), Dr. Takaki Onozato (OB, SONY), Dr. Xi Zhang (OG, Professor at CQUT), Dr. Prashant Ghediya (OB, Sharp), Dr. Gowoon Kim (OG, SAMSUNG), Dr. Doudou Liang (OG, Professor at Ludong U), Dr. Mian Wei (OG, Henan U.), Dr.Qian Yang (OG, Professor at Jiangsu U.), Dr. Binjie Chen (OB, specially appointed associate researcher at Wuzhen Lab), Dr. Hui Yang (OG, Professor at Shenzhen Technology U.), Dr. Lizhikun Gong (OB, Postdoc at Wuhan University), Dr.

Zhiping Bian (OB. Micron Memory Japan), Dr. JEONG, Ahrong (Postdoc. RIES, Hokkaido U.), Mr. Kungwan Kang (Ph.D candidate, IST, Hokkaido U.), Mr. ZHOU, Weikun (Ph.D candidate, IST, Hokkaido U.), Mr. Kong, Hyeonjun (Ph.D candidate, IST, Hokkaido U.), Mr. Kenyu Sugo (OB), Mr. Yugo Takashima (OB), Mr. Takashi Fujimoto (OB), Mr. Liao Wu (OB), Mr. Rui Yu (OB), Mr. Yaoming Liu (OB), Ms. Mitsuki Yoshimura (Master candidate, Hokkaido U.), Ms. Marunouchi, Ko (Master candidate, Hokkaido U.), Ms. SADAHIRA, Hikaru (Master candidate, Hokkaido U.), Ms. Ozaki, Ms Ishino, Ms, Kasuga (Secretary, Ohta lab) *et al*. for all the countless help during my study and life. Special thanks to Dr. Yuqiao Zhang for teaching me the manipulation of facilities in Ohta lab as well as lots of helpful scientific discussions, Dr. Prashant Ghediya help me on discussion about the current research, and Dr. Jeong, Ahrong encourage me in my tough time.

I really appreciate the collaborations from Prof. Matsuo (Hokkaido U.) for ICP-MS measurement, Prof. Feng (U. Tokyo) for STEM observations of IGZO superlattice, Prof. Matsuda (Hokkaido U.) for ultrafast phonon speed measurement. I also appreciate the thesis committee members, Prof. Tetsuya Uemura (IST, Hokkaido U.), Prof. Seiya Kasai (RCIQE, Hokkaido U.) and Prof. Taketomo Sato (RCIQE, Hokkaido U.) for taking time to review this thesis and giving me valuable comments.

Thirdly, I do the deepest appreciate to my parents and grandparents. Thanks to their support and tolerance for my trouble and immature. Also, I am extremely grateful to Dr. Ishii (SACC), I am not even sure whether I could get over the toughest time without her support.

Lastly, I'm grateful to the financial support provided by the China Scholarship Council.

List of Publications

Papers related to the given thesis

[1] **Wu, Y.**, Magari, Y., Ghediya, P. R., Zhang, Y., Matsuo, Y., & Ohta, H. (2024). High-mobility and high-reliability Zn-incorporated amorphous In_2O_3-based thin-film transistors. *Japanese Journal of Applied Physics*, *63*(7), 076504.

[2] **Wu, Y.**, Ghediya, P. R., Zhang, Y., Matsuo, Y., Ohta, H., & Magari, Y. (2024). Thermopower modulation analyses of effective channel thickness for Zn-incorporated In_2O_3-based thin-film transistors. *Japanese Journal of Applied Physics.*

Other papers

[1] Krahl, F., **Wu, Y.**, Cho, H. J., Karppinen, M., & Ohta, H. (2020). Spontaneous Generation of Carrier Electrons at the Interface between Polycrystalline ZnO and Amorphous $InGaZnO_4$. *Advanced Electronic Materials*, *6*(10), 2000404.

[2] Cho, H. J., **Wu, Y.**, Zhang, Y. Q., Feng, B., Mikami, M., Shin, W., ... & Ohta, H. (2021). Anomalously Low Heat Conduction in Single-Crystal Superlattice Ceramics Lower Than Randomly Oriented Polycrystals. *Advanced Materials Interfaces*, *8*(7), 2001932.

[3] Cho, H. J., **Wu, Y.**, Kwon, Y., Qi, J., Kim, Y., Saito, K., & Ohta, H. (2021).

Anisotropic heat conduction of coherently transported phonons in $InGaO_3(ZnO)_m$ single crystal films with superlattice structures. *arXiv preprint arXiv:2108.04970*.

[4] Qi, J., **Wu, Y.**, Cho, H. J., Kim, Y., Ohta, H., & Tamaoki, N. (2021). Pressure-tunable thermal conductivity observed for bisamide functionalized diacetylene crystals. *Journal of Materials Science*, *56*(27), 15481-15490.

[5] Cho, H. J., **Wu, Y.**, Qi, J., Kim, Y., Ohta, H., & Matsuda, O. (2022). Specular Acoustic Vibrational Wave Transmissions with the Presence of Phononic Bandgaps. *Journal of the Physical Society of Japan*, *91*(1), 014601.

List of Presentation

[1] Mini workshop on functional materials science (organizers' meeting)

December 1st - 2nd, 2023

“Modulation of Electron Transport Properties of Amorphous In−Zn−O Films with Varied Zn Concentration”, (Poster)

[2] The 24th RIES-HOKUDAI International symposium

“Modulation of Electron Transport Properties of Amorphous In−Zn−O Films with Varied Zn Concentration” (Poster)

[3] 第59回 応用物理学会北海道支部/第20回 日本光学会北海道支部 合同学術講演会プログラム

“Modulation of Electron Transport Properties of Amorphous In−Zn−O Films with Varied Zn Concentration” (Oral)

[4] 第71回応用物理学会春季学術講演会

“Role of Zn Introduction in In_2O_3 TFTs − Suppression of Grain Boundary Scattering −” (Oral)

[5] The 79th Japan Society of Applied Physics Fall Meeting

Period modulated thermal conductivity of $InGaO_3(ZnO)_m$ (m = integer) single crystalline

thin films (Oral)

[6] The 20th RIES-HOKUDAI International Symposium

Thermal conductivity of $InGaO_3(ZnO)_m$ (m = integer) natural superlattice (Poster)

[7] RIES-NCTU Workshop

Thermal conductivity of $InGaO_3(ZnO)_m$ (m = integer) natural superlattice (Poster)

[8] The 3rd Workshop on Functional Materials Science, Sapporo, Japan, December 18th-20th, 2019.

Phonon propagation competition across natural superlattice $InGaO_3(ZnO)_m$ (Poster)

[9] The 55th Japan Society of Applied Physics Hokkaido branch meeting

Anisotropic heat transport of natural superlattice oxide $InGaO_3(ZnO)_m$. (Oral)

[10] The 68th Japan Society of Applied Physics Spring Meeting

Anomalously Low Heat Conduction in Single-Crystal Superlattice Ceramics Lower than Randomly Oriented Polycrystals (Oral)